ADAS-EU R(12)SU03

ADAS-EU
ADAS for fusion in Europe

Grant: 224607

Martin O'Mullane

ITER1: ITER visits and support activities
Report 1

10 Feb 2012

Workpackages : 2-3 and 3-4
Category : DRAFT – CONFIDENTIAL

ITER1: ITER visits and support activities
Report 1

Martin O'Mullane

Department of Physics, University of Strathclyde, Glasgow, UK

Abstract: *Visits and support actions, on-site and off-site, provided under ADAS-EU to the ITER Organization in the reporting period: months 19-36.*

Contents

Chapter 1

Overview

An important goal of the Support Action was to strengthen the atomic physics base required for ITER. The project has enabled the active participation of ADAS-EU staff with the design activities of the ITER diagnostic group and a significant engagement with the ITER physics team. The working relations, fostered by ADAS-EU, was considered to be successful and from October 2011 ITER is now directly funding this activity thus freeing up resources for other ADAS-EU activities.

The principal activity is the forward modelling of expected emission to aid spectroscopic design. VUV, X-ray and visible systems viewing the upper part of the plasma, main plasma survey systems and divertor monitors in the visible, X-ray and VUV have been considered. These share a commonality in plasma scenario and transport modelling but can have quite different atomic physics needs. Although there is a large overlap in atomic data needs between ITER and present day machines the conditions in ITER and its plasma facing components have necessitated the calculation of atomic data not already present in ADAS. These new data will be made available to ADAS, and to the wider community via OPEN-ADAS, with suitable acknowledgment to ADAS-EU.

This report gives a brief overview of the common plasma scenarios and transport models followed by the more specific atomic data needs of the diagnostic systems considered. The information outlined here is incorporated into the detailed design documents (DDD) and has been presented at a number of conceptual design reviews (CDR) the first approval stage for ITER diagnostics. It is necessarily limited to the atomic and emission modelling aspects of the design. The visits and CDR dates are given in the appendix.

Note that a tailored ADAS-EU course was delivered at ITER in December 2010; details can be found in the dissemination report (ADAS-EU R(11)DI02).

Chapter 2

ITER plasma scenarios

2.1 Magnetic geometry and background plasma profiles

Modelling the impurity emission requires a defined background plasma. In present day machines the magnetic geometry and plasma electron temperature and density profiles are measured. For ITER these are necessarily taken from models which are compatible with the defined measurement requirements and the current thinking on plasma performance. Official ITER models are used when available although others can be utilized to explore a greater parameter space. A diagnostic must be designed to be able to measure data from plasmas other than the best performing reference scenario. The response of the diagnostic to start-up, steady-state and ramp-down plasmas during the low-activation, DD and full exploitation (DT) phases of ITER must be considered.

The magnetic geometry is converted from EFIT EQDSK [1] files from ASTRA [2] models which is the same format as produced by the EFIT measured data from JET, DIII-D, K-STAR and other tokamaks.

The electron and ion temperature and electron density profiles are taken from ASTRA or CORSICA [3] code runs. These models consider impurities in a rudimentary fashion in order to attain the assumed Z_{eff} but are unsuitable for predicting the impurity emission required for spectroscopy diagnostic design.

The following scenarios are considered:

Scenario
15MA inductive burn
7.5MA H-mode
10MA H-mode ramp-up
10MA H-mode ramp-down
10MA L-mode ramp-up
15MA QDT=10 flat density profile
15MA QDT=10 peaked density profile
13.8MA hybrid scenario 3 with sawteeth
15MA QDT=10 flat density profile with ELMs

The first scenario in the list is the standard ITER reference inductive burn scenario at 15MA and is catalogued in the ITER internal document system as part of the Plant Breakdown Structure. The others scenarios are variations provided by the ITER FST group. All scenarios describe the ITER plasma at one time point but the sawtooth and ELM results describe the temperature and density profiles before and immediately after the disruptive event.

The CORSICA and ASTRA scenarios only consider the confined plasma so a 10cm exponential fall-off in the SOL for both temperature and density (to a minimum of 50eV and $10^{16}m^{-3}$ respectively) has been imposed.

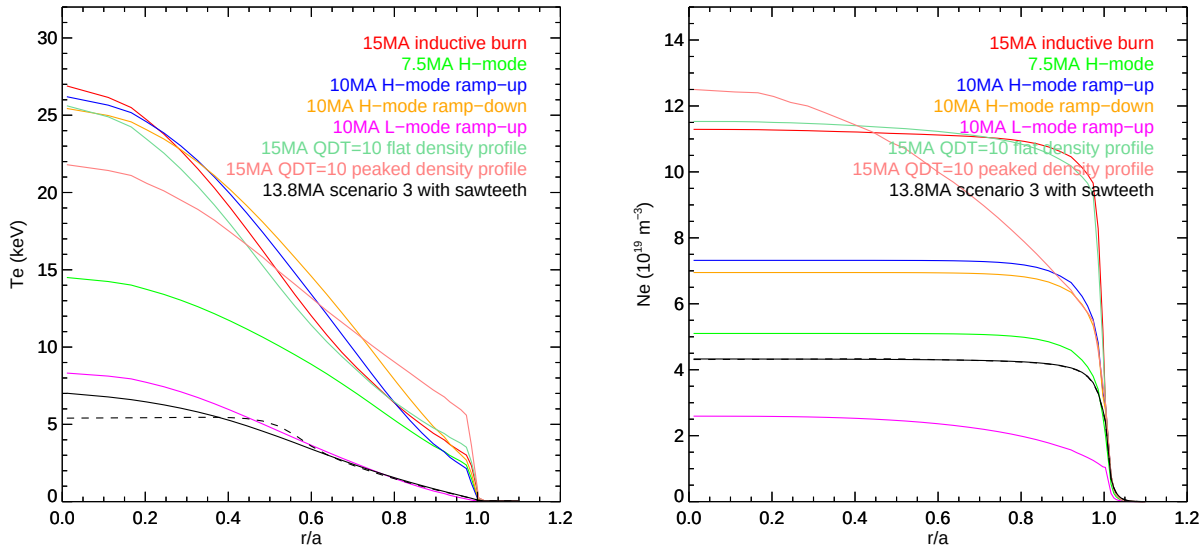

Figure 2.1: Electron temperature and density profiles for various plasma scenarios. The dashed line shows the profile immediately following the sawtooth crash. Note there is no change in density at the crash.

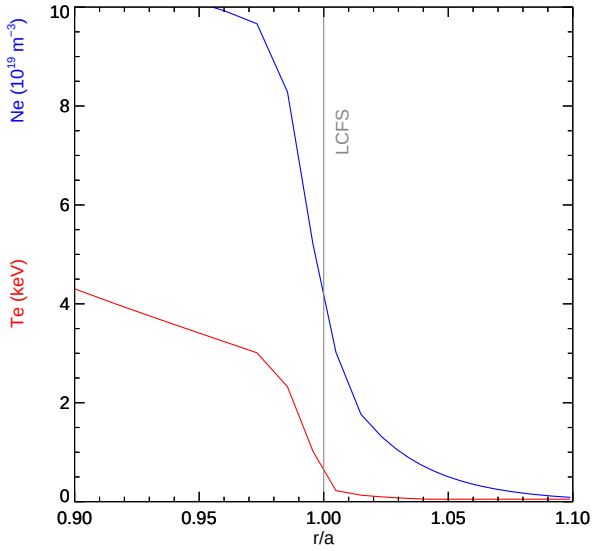

Figure 2.2: Electron temperature and density profiles SOL behaviour added to ITER standard models.

2.2 Impurity transport model

The SANCO impurity transport code is used to produce the distribution of ionisation stages in the ITER scenarios. The code assumes axisymmetry and the magnetic flux surfaces define the geometry. It solves for radial transport in flux-space.

The particle flux is described by diffusive (D) and convective (V) terms:

$$\begin{aligned}\Gamma_k &= -D\langle|\nabla\psi|^2\rangle\frac{\partial n_k}{\partial\psi} + v\langle|\nabla\psi|\rangle n_k \\ &\equiv -D^*\frac{\partial n_k}{\partial\psi} + v^* n_k\end{aligned}$$

where for each ion stage, k, the same transport as a function of (poloidal) flux surface (ψ) is used.

Transport determines the impurity distribution in the plasma which directly affects where the radiation is emitted. The code solves the set of equations:

$$\begin{aligned}\frac{\partial N(z)}{\partial t}+\frac{\partial \Gamma(z)}{\partial \psi} &= S^{z-1\rightarrow z}n_e N(z-1)\\ &\quad -\left(\alpha^{z\rightarrow z-1}+S^{z\rightarrow z+1}\right)n_e N(z)\\ &\quad +\alpha^{z+1\rightarrow z}n_e N(z+1)\end{aligned}$$

where S is the ionisation rate and α is the (radiative + dielectronic) recombination rate.

The source of the impurities is specified as a time-dependent influx rate.

SANCO assumes that the dominant populations are in the ground state of each ionisation stage and that the excited states, the decay of which give rise to the emission, are in quasi-static equilibrium with them. Therefore the emission rates are functions of the local temperature and density.

The plasma electron temperature and density profiles are specified as inputs. These profiles, and the plasma magnetic geometry, can vary in time and the SANCO model can operate with time varying background profiles. Note that the impurities are considered as trace particles so any change in the impurity content or distribution is not used to alter the temperature and density profiles as the simulation evolves.

2.3 Transport coefficients adopted for the simulations

There are no robust empirical rules to predict the impurity transport coefficients. However, it is possible to extrapolate from existing machines.

Over a wide range of JET operation scenarios the measured transport coefficients fall into a set of bands.

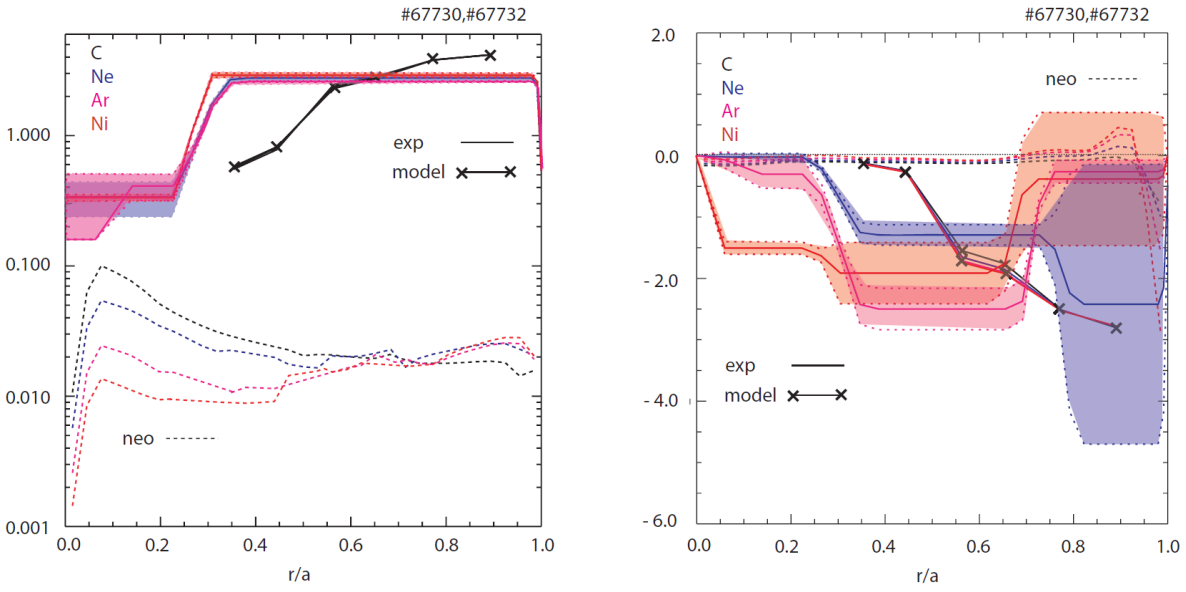

Figure 2.3: Impurity transport coefficients for JET scenarios, presented at the ITPA T&C Meeting, Culham, March 2010 (C. Giroud).

The estimation of a forward modelled signal for diagnostic design should *not* be marginal relative to the transport coefficients. The relatively narrow range of values for a variety of JET plasma types suggests that a global D and V can be used for ITER diagnostic design.

The following coefficient have been adopted:

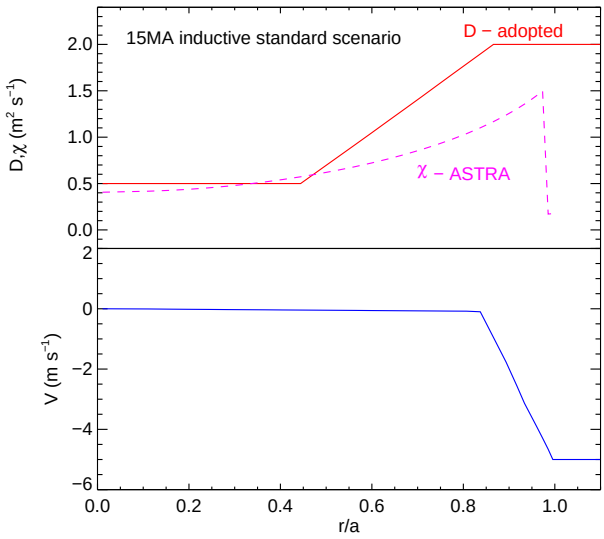

Figure 2.4: Effective or compromise coefficients used for impurity transport models. The diffusion coefficient is compared to the ASTRA energy transport profile.

2.4 Sensitivity of emission model to transport

It is imperative that the diagnostic design is useful for a range of possible plasmas. The transport coefficients are one of the less precisely specified inputs to the models. However most ITER plasmas will have a flat density profile so if the dependence of the transport model to a wide range of coefficient is modest then the design can proceed with confidence. Interpretation of results from the measurements made by such a diagnostic is a different matter but in that situation the transport is likely to be one of the plasma characteristics being sought.

The minimal transport is one of infinite confinement. Figure 2.5 shows that transport broadens the width of the emission shells but does not radically shift them from their local condition positions. The shift is well with the operating range of a diagnostic.

Figure 2.6 shows the effect of a very wide range of possible transport coefficients on the carbon impurity density. In all cases the concentration within the confined plasma is 1% of carbon but its shape can be altered by extreme transport.

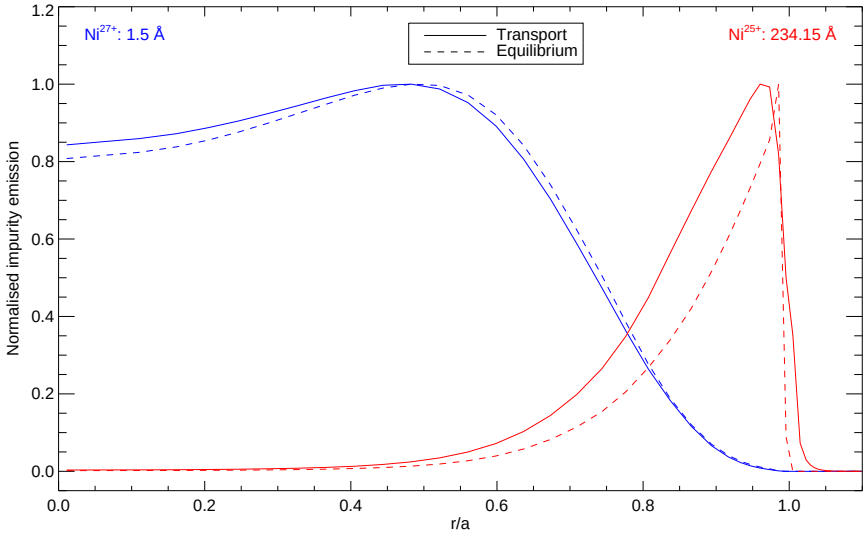

Figure 2.5: Effect of transport on X-ray He-like nickel lines in the standard high performance ITER scenario.

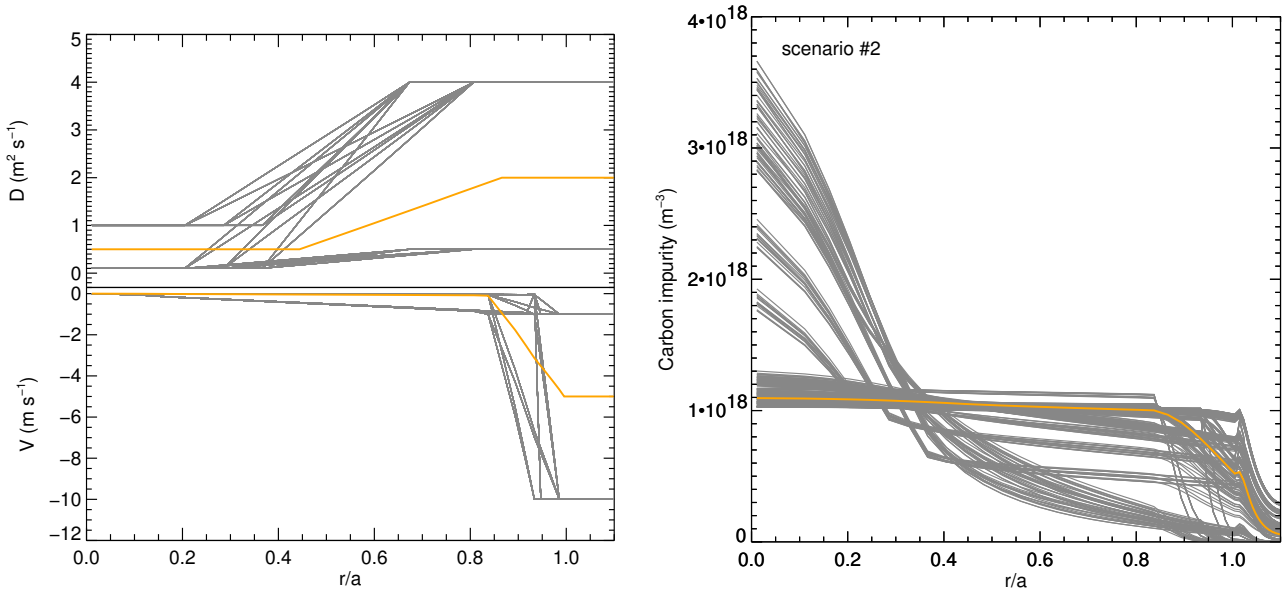

Figure 2.6: Effect of large changes in transport coefficient on the impurity profile of 1% carbon in the standard high performance ITER scenario. The highlighted coefficient are the ones used throughout the report.

2.5 Plasma models of SOL and divertor

The plasma in the scrape off layer and divertor must be modelled in a 2D geometry and is not possible to simplify it as in the confined plasma as describe earlier. There is an activity at ITER to model the edge plasma since this boundary largely determines the performance. The SOLPS, ERIENE and OSM plasma transport codes are used to generate a 2D description of the boundary plasma with an assumption of toroidal symmetry.

There are a number of SOLPS runs, available from the ITER physics group, based on low, medium and high neutral pressure within the operational window envisaged for ITER performance. For the purpose of diagnostic design we take these as inputs. Figure 2.7 shows the extent of the solution grid and a profile of the temperature and density along a line of sight through the X-point. The SOLPS calculations do not match the reference scenario where the core

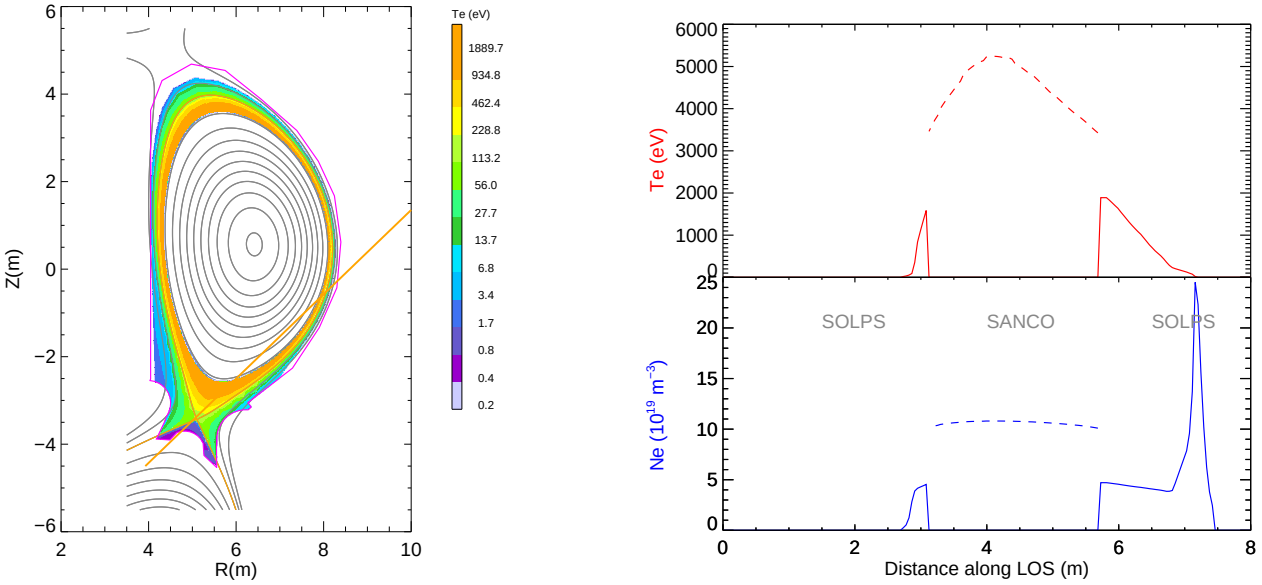

Figure 2.7: (left) Spatial extent of the SOLPS solution. (right) Profile of temperature and density along a LOS through the X-point. The dashed line shows the mis-match between the SOLPS and reference scenario solutions.

ASTRA profile and edge SOLPS profiles merge. Although the SOLPS models are consistent with the ITER Heat and Nuclear Load Specifications, matching the inner/core boundary of the model is not a priority yet.

Chapter 3

Edge VUV Imaging

3.1 Instrument and wavelength range

The upper port imaging VUV spectrometer purpose is to view the edge of the plasma without being swamped by emission from the divertor. The VUV region has strong emission lines from metallic and light element elements and is a good proxy measurement for localised radiated power. The location of the instrument is:

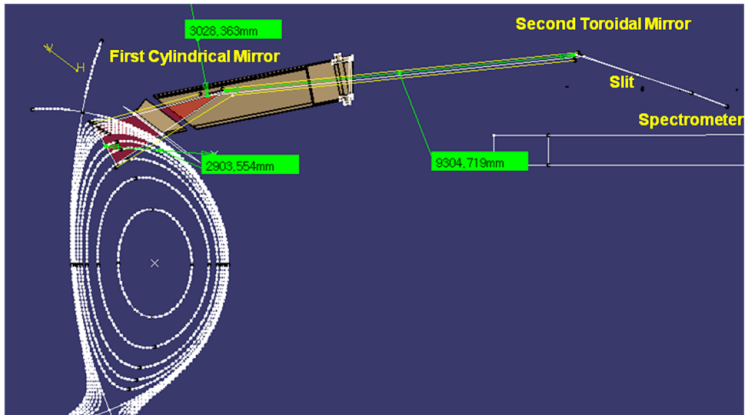

A wavelength region, 215–260Å was identified which contained emission from the principal radiators. It is narrower than typical VUV instruments but one of the measurement requirements is to determine ion temperature s the line shape is important. A number of prominent impurity lines were identified and the contribution to the overall power and their temperature of peak (coronal) abundance are given in table 3.1.

3.2 Emission predictions

The local emissivities with a realistic impurity mix of table 3.2 are shown in figure 3.2.

The instrument will be imaging rather than a single line of sight with the outermost chord seeing very little of the confined plasma. The change in line of sight integrated emission is key to assessing the capability of the diagnostic. Figure 3.2 compares the LOS intensities of carbon, nickel and tungsten lines over the expected chordal sweep of the instrument. As expected the peak of the emission varies with the element atomic number and the figure is used to determine how deep into the plasma the innermost chord needs to be.

Ion	Suggested				Power Contribution	
	λ(Å)	Transition			% stage	at equil. Te
He II	256.32	$1s\,^2S$	–	$3p\,^2P$	3.29	4.5
Be IV	256.30	n = 6	–	2	0.47	15.0
C IV	244.91	$1s^22s\,^2S$	–	$1s^24p\,^2P$	0.01	7.2
C V	227.19	$1s2s\,^3S$	–	$1s3p\,^3P$	0.66	30.3
C V	247.32	$1s2s\,^1S$	–	$1s3p\,^1P$	0.01	30.3
C V	248.70	$1s2p\,^3P$	–	$1s3d\,^3D$	0.67	30.3
N IV	247.21	$1s^22s^2\,^1S$	–	$1s^22s3p\,^1P$	0.11	8.0
O V	215.15	$1s^22s2p\,^3P$	–	$1s^22s3s\,^3S$	3.16	14.5
Ar XV	221.15	$2s^2\,^1S_0$	–	$2s2p\,^1P_1$	67.98	286.8
Cr XXII	223.02	$1s^22s\,^2S_{1/2}$	–	$1s^22p\,^2P_{3/2}$	13.68	942.7
Fe XXIV	255.11	$1s^22s\,^2S_{1/2}$	–	$1s^22p\,^2P_{1/2}$	14.70	1681.7
Ni XVII	249.18	$2p^63s^2\,^1S_0$	–	$2p^63s3p\,^1P_1$	96.17	229.0
Ni XXVI	234.15	$1s^22s\,^2S_{1/2}$	–	$1s^22p\,^2P_{1/2}$	21.92	1852.0
Cu XVIII	234.20	$2p^63s^2\,^1S_0$	–	$2p^63s3p\,^1P_1$	72.74	277.8
Cu XXVII	224.79	$1s^22s\,^2S_{1/2}$	–	$1s^22p\,^2P_{1/2}$	13.10	1975.0
Kr XXVI	220.06	$3s\,^2S_{1/2}$	–	$3p\,^2P_{1/2}$	29.03	1038.2

Table 3.1: The stronger VUV lines expected in the 215–260Å region.

Impurity	Concentration (%)	Radiated power (MW)	
		core	SOL
He	4.0000	2.08	0.04
Be	2.0000	5.19	0.19
C	0.5000	3.52	0.15
O	0.1000	1.49	0.08
Ar	0.1200	20.78	0.68
Fe	0.0100	6.40	0.10
Ni	0.0100	5.20	0.15
W	0.0001	0.86	0.01
Z_{eff}	1.90		

Table 3.2: A realistic mix of impurities for ITER.

One of the concerns for spectroscopic diagnostics in ITER is the contamination of the spectrum by tungsten as it produces quasi-continuum line emission in many part of the spectrum. The levels are expected to be low but figure 3.2 shows some of the complexity which indicates that treating it as an additional simple contribution to the background is not sufficient.

The ITER measurement requirements are a little more arbitrary and demand that the instrument should be capable of observing impurities at a concentration of 0.5% when $Z < 10$ and at the 0.01% level for heavier elements. Figure 3.2 compares the local emissivities at these concentrations.

One of the disadvantages of the wavelength region chosen is that the strongest beryllium line is the $n = 6 - 2$ Balmer line which will be blended with the Helium $n = 3 - 1$ Lyman line. Figure 3.2 shows that the emissivity of the He is significantly greater than the Be and the masking will be enhanced when the helium content is large. Choosing this range excludes the possibility of monitoring beryllium with this diagnostic.

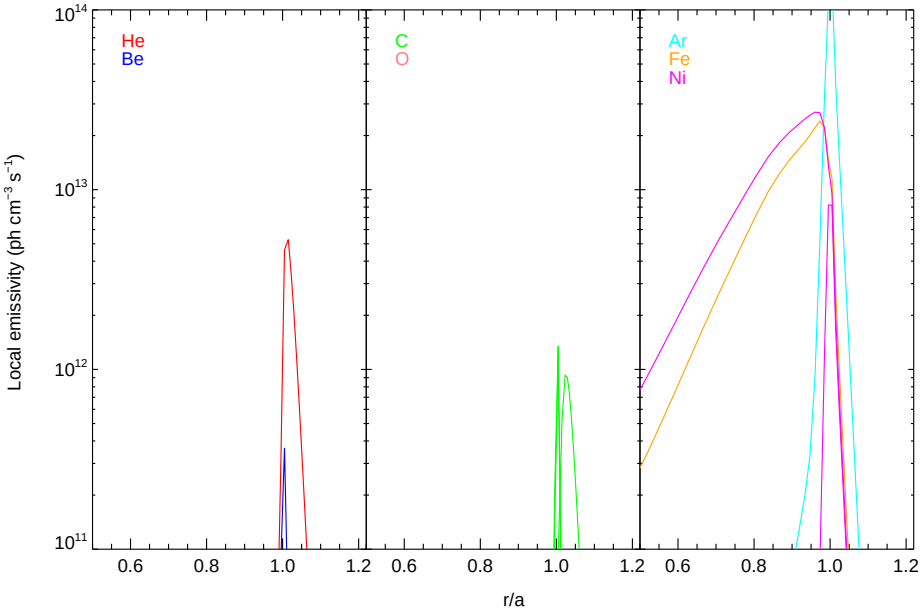

Figure 3.1: The local VUV emission profiles of likely ITER impurities.

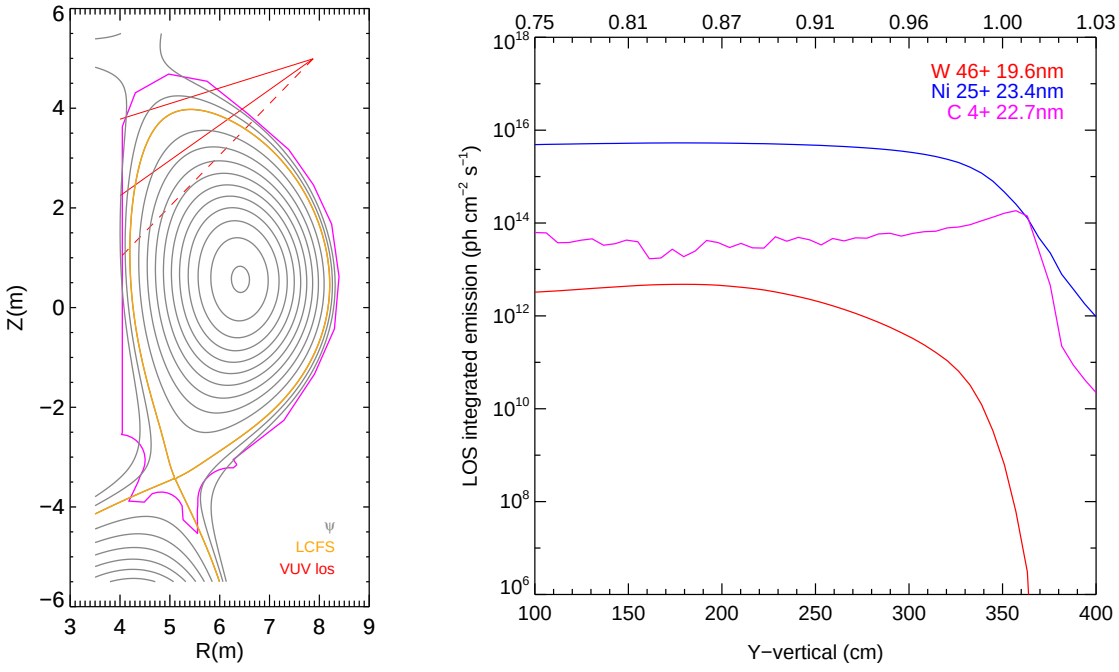

Figure 3.2: Inward extent of emission shells of intrinsic impurities. (left) The red lines denote the current extend of the instrument view with the dotted line showing the maximum possible given the current port and mirror position constraints. (right) LOS integrated emission labels by vertical displacement (lower axis) and impact radius in flux space (top axis) for intrinsic impurities. Concentrations of 0.1%c, 0.01% Ni and 10^{-5} W are assumed.

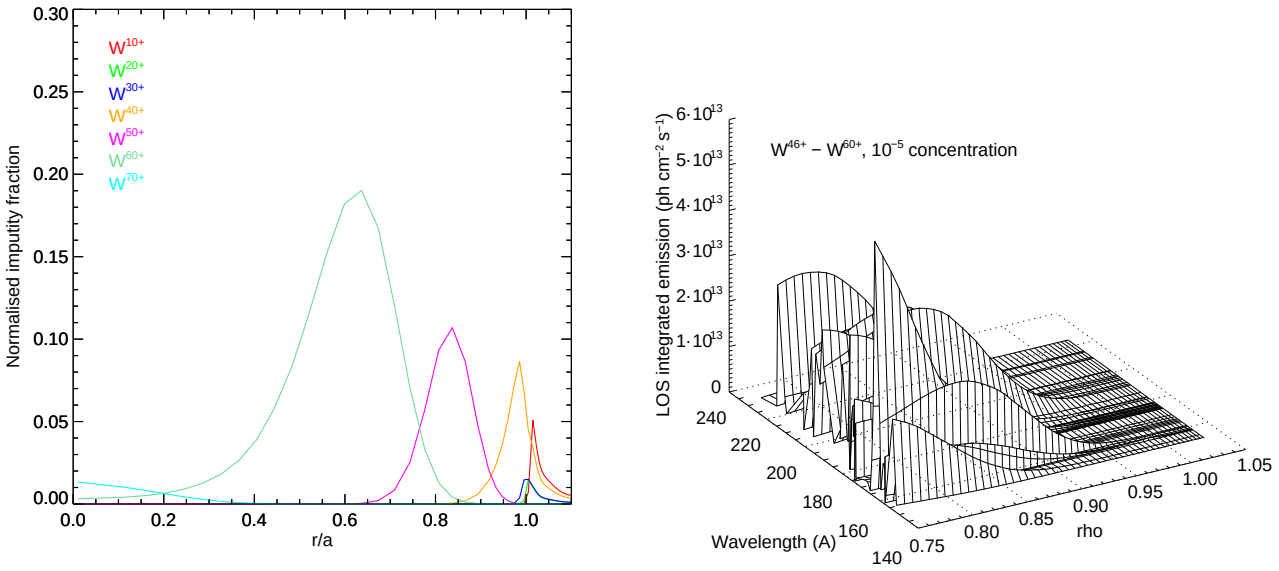

Figure 3.3: The strongest lines of tungsten contributing to the LOS integrated spectrum.

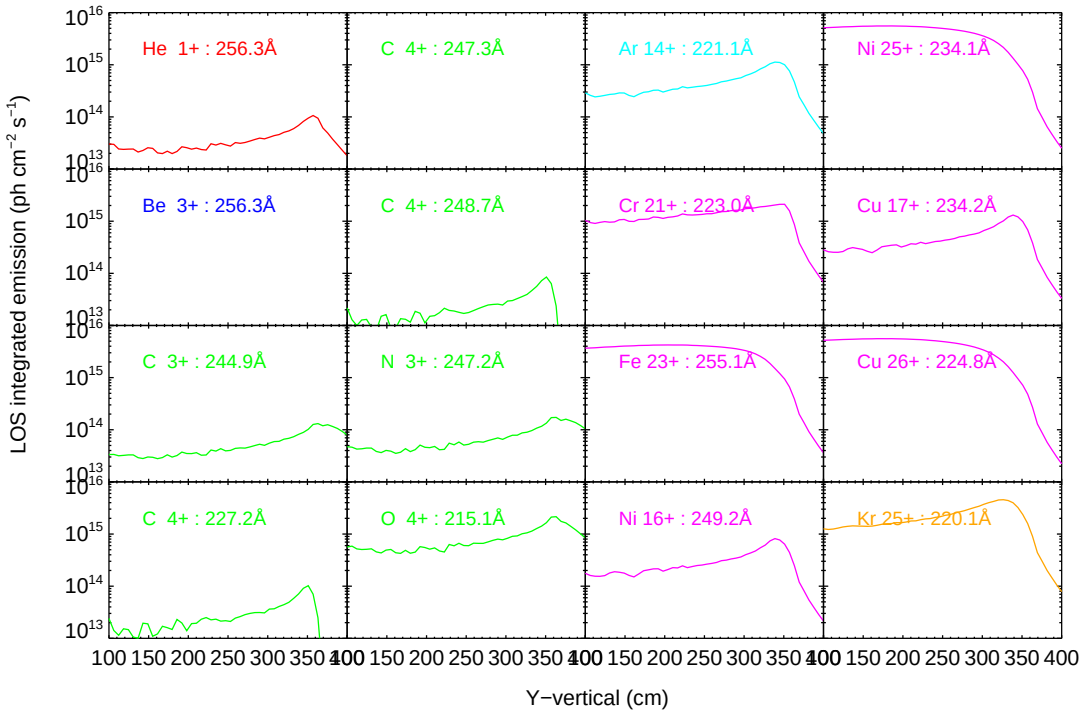

Figure 3.4: Comparison of LOS integrated emission for the ITER measurement requirement concentrations. For this concentration Be will be very difficult to measure.

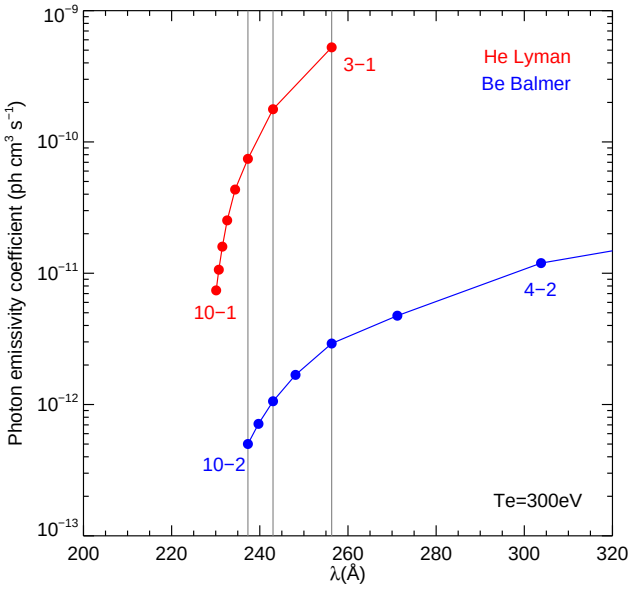

Figure 3.5: Photon emissivities of the He Lyman series compared to the Be Balmer series at an edge temperature likely in ITER.

Chapter 4

VUV core survey spectrometer

4.1 Instrument

The VUV core survey spectrometer is one of three VUV subsystems that together monitor the ITER core, edge and divertor plasmas. Its primary role is to measure impurity ion radiation and to identify all relevant impurities in ITER main plasma. The VUV core survey spectrometer monitors the plasma through an equatorial port has been designed as a 5-channel spectral system with high efficiency, so that the high spectral resolution of several hundred could be achieved in the wide range of wavelength of 24–1600Å.

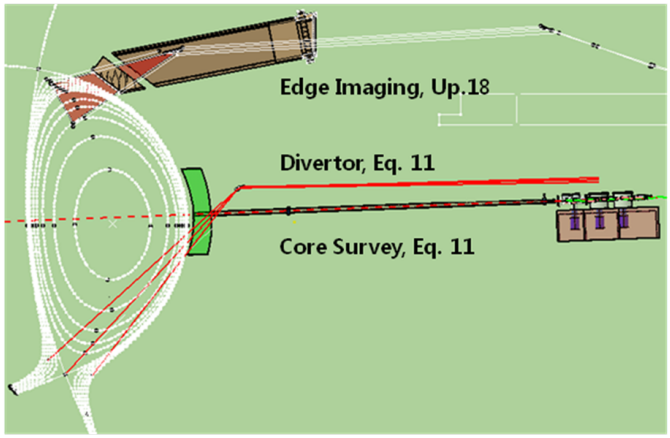

A survey spectrometer is expected to measure the presence of elements with $Z > 1$ and global estimates of these elements must be obtained continuously, not only for physics reasons, but also for the first-wall protection (*eg* Cu spectral lines would imply damage). The absolute quantity of the impurity species as well as their rate of increase is required by the measurement requirements.

- Vessel materials and plasma facing components
  — Be, C, Cr, Fe, Ni, W
- Intrinsic and control gases
  — N, O, Ne, Ar
- In-vessel component materials
  — Mg, Al, Si, Ca, Cu
- Mirrors
  — Mo, Rd, Au
- Anything else, *eg* results of transmutation!
  — Cd, Re

4.2 Possible emission lines

A database of photon emissivity coefficients for a set of possible impurities was assembled, extending the size of the ADAS *adf15* database. The number of transitions considered in the 100–1600Å region is given in table 4.2.

He	9	N	235	Mg	39
Be	29	O	259	Al	45
C	198	Ne	290	Si	244
Fe	347	Ar	410	Ca	93
Ni	312			Cu	49
Cr	61				
W	941				

Table 4.1: Number of transition lines considered in the VUV region. Each line has an accompanying photon emissivity coefficient.

However not all of these will be strong and the permitted synthetic spectrum is given in figure 4.2 for a slightly higher than anticipated Z_{eff} of 2.1.

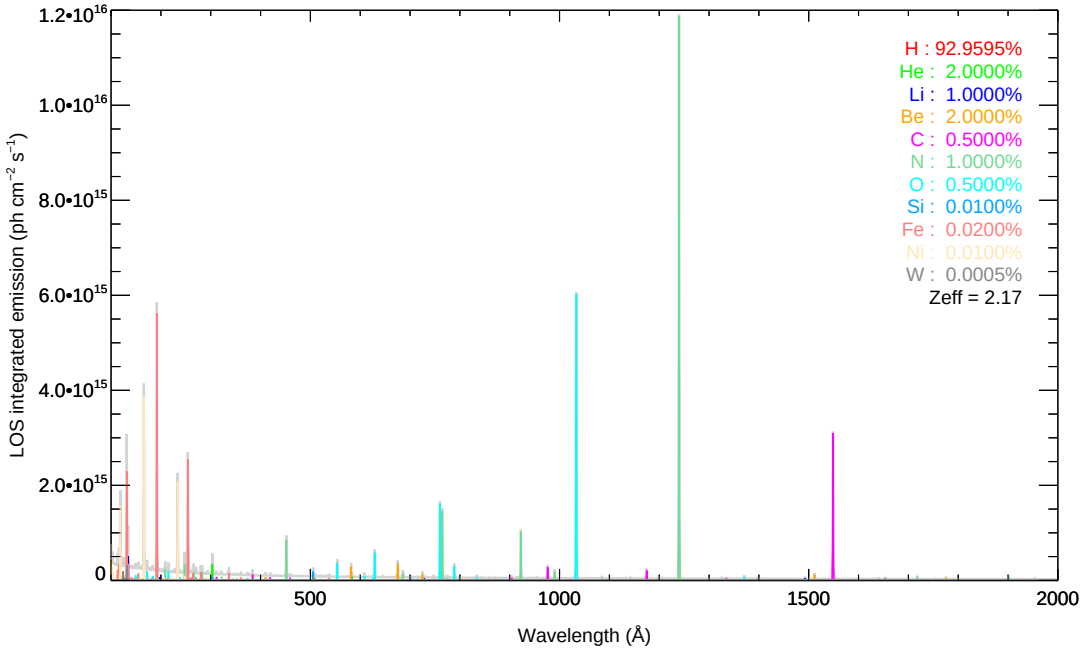

Figure 4.1: Line of sight integrated spectrum in the VUV region for a wide range of impurities..

Chapter 5

VUV divertor survey spectrometer

5.1 Instrument

The divertor VUV instrument views the outer leg of the divertor as far as the X-point via an equatorial port view. It is of a similar design to the core VUV but monitors a narrower spectral range between 150–320Å.

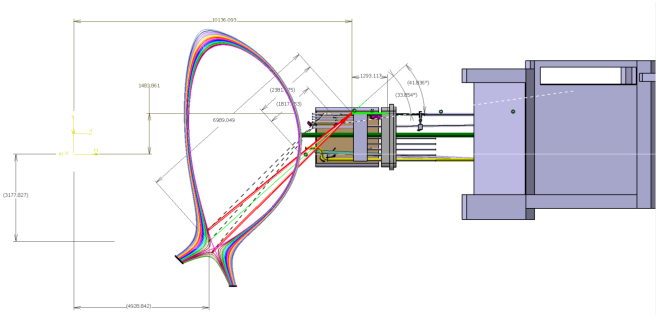

The SOLPS model of the edge plasma was used for the background plasma with the (mismatched) reference plasma for the core. The ITER divertor plasma facing components are carbon in the vertical strike plates and tungsten elsewhere. Predictive emission modelling is used to assess the intensity of both these elements and the contribution to the line of sight emission of contributions from the divertor and confined plasma. The SOLPS simulations include a carbon impurity transport model but do not have one for tungsten. Therefore the tungsten is modelled by using an equilibrium ionisation balance with the implicit assumption that transport among the stages contributing to the emission have a modest effect, at least for the purposes of diagnostic design. The fractional abundance along a LOS through the X-point is show in figure 5.1.

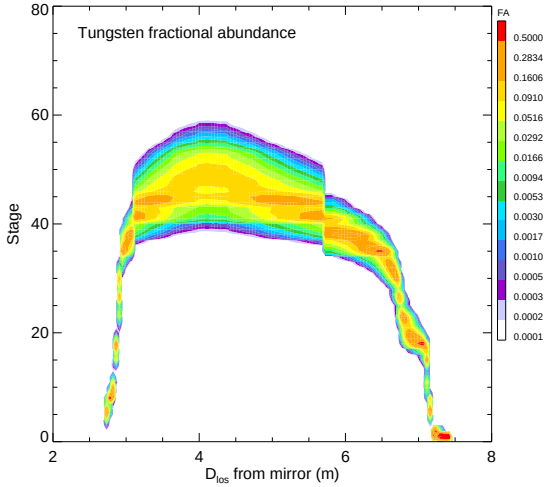

Figure 5.1: (Coronal equilibrium) fractional abundance of tungsten along a line of sight from mid plane through the X-point.

5.2 Synthetic spectra

The emission at the extremes of the spectrometer view are shown for carbon in figure 5.2 and tungsten in figure 5.2. Note that in both figures the impurity concentration is normalized to 1%, an unrealistic value for tungsten but is chosen to allow simple scaling between elements.

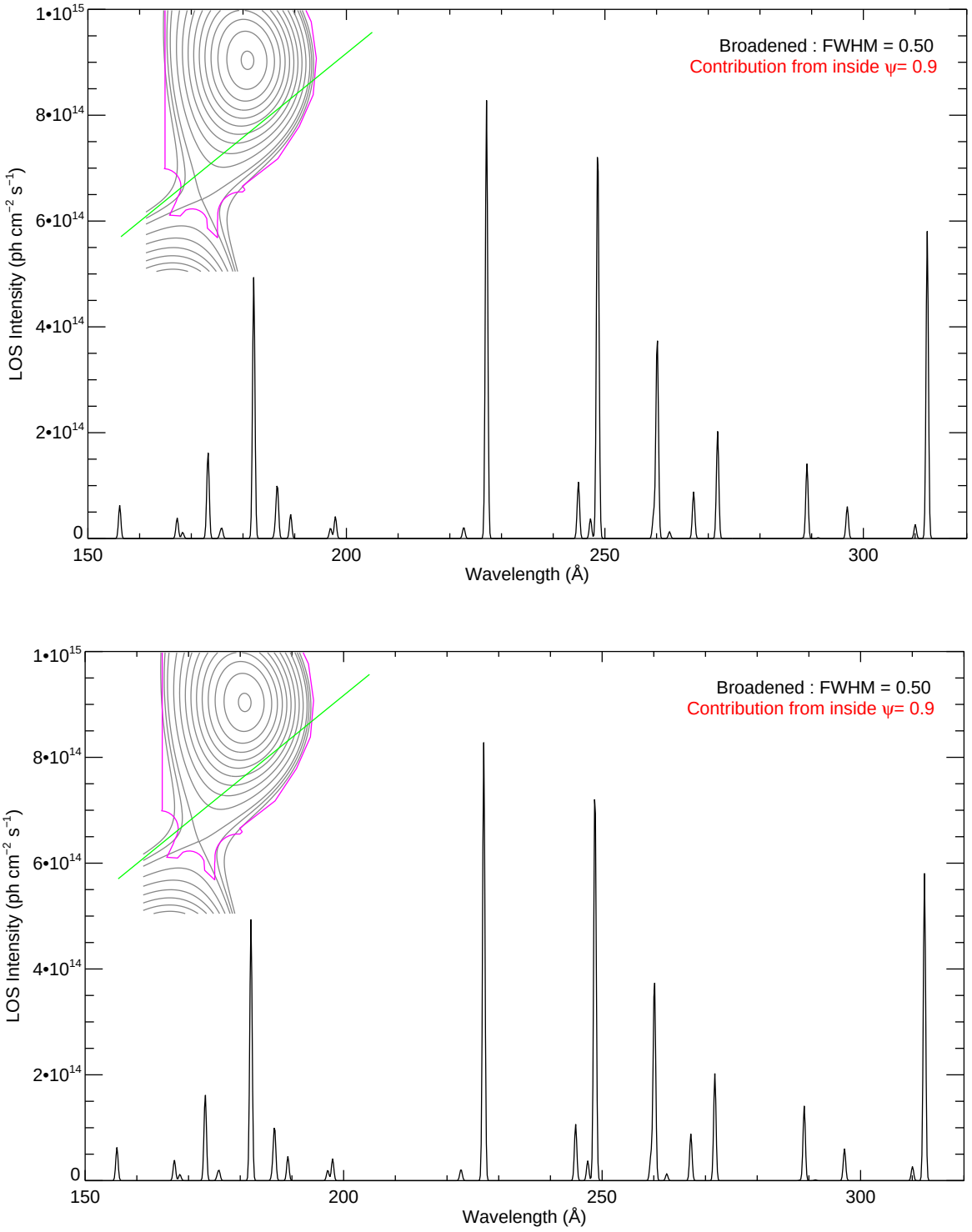

Figure 5.2: LOS intensity of carbon emission from divertor region with an assumed core concentration of 1%.

It is necessary to consider contaminating emission from the core confined plasma when interpreting the spectrum form tungsten but this is not a consideration for the lighter elements such as carbon.

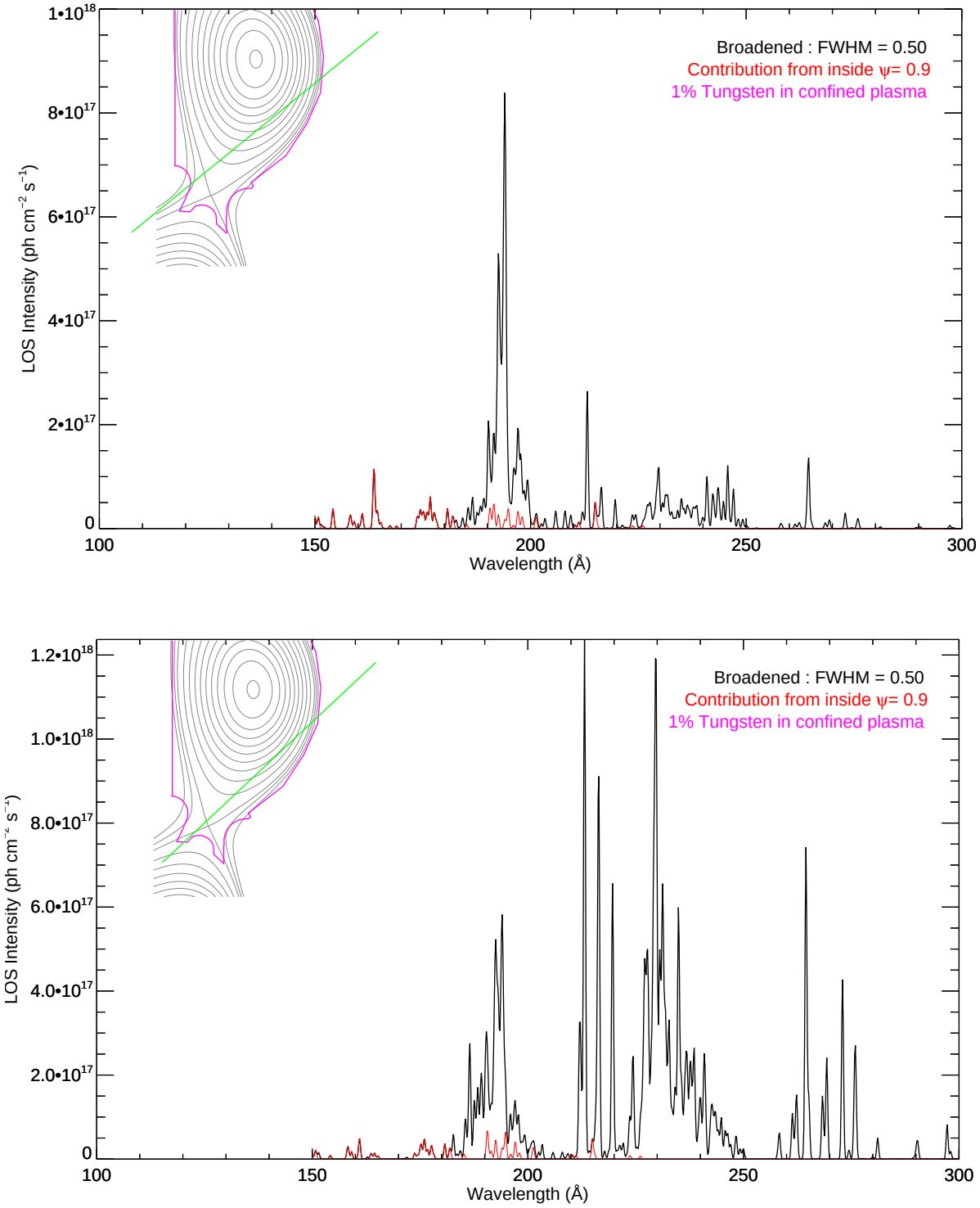

Figure 5.3: LOS intensity of tungsten emission from divertor region with an assumed core concentration of 1%.

Chapter 6

Upper port X-ray spectrometer

6.1 Instrument and lines of sight

The Upper Port X-ray Imaging spectrometer is part of an array of imaging x-ray crystal spectrometers that together view the full ITER poloidal profile. Its primary goal is to measure ion temperature and plasma rotation profiles in the outer plasma. A poloidal region of the plasma at $r/a > 0.9$ is imaged via a spherical crystal placed outside of an upper port, onto the 2-D X-ray detector. It is optimized for very high spectral resolution in a narrow band around wavelengths 2–5Å interval, chosen to contain representative line emission from the main impurities.

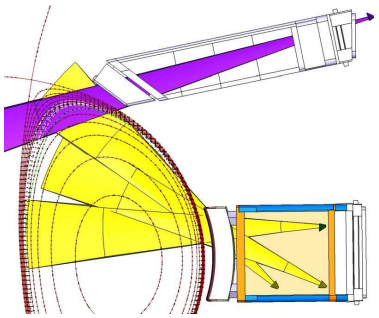

The fractional abundance of tungsten along the lines of sight of the instrument is shown in figure 6.1.

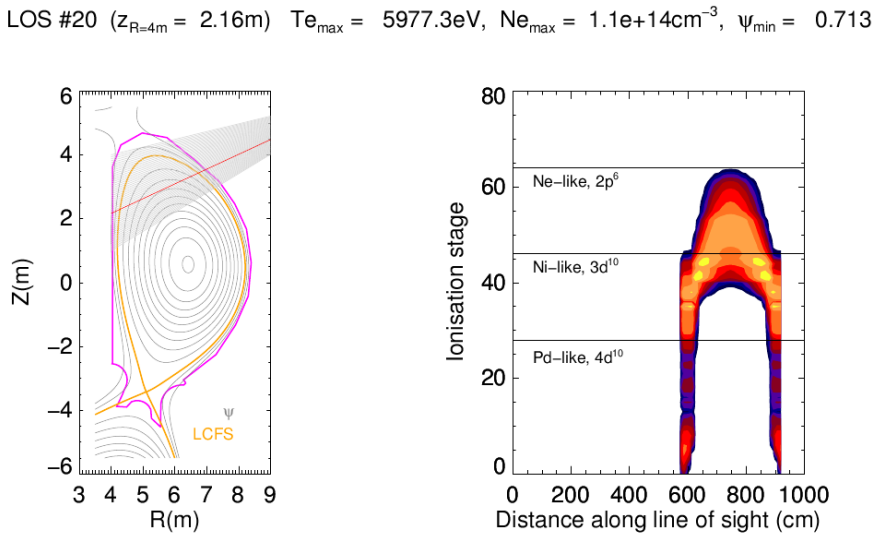

Figure 6.1: Fractional abundance of tungsten along one of the possible LOS.

6.2 Tungsten emission line in X-ray region

A survey of the strongest lines in the 2–8Å region, ranked by the maximum photon emissivity at the temperature of maximum abundance of the stage in the ADAS *adf15* collection, returns 708 distinct lines arising from stages W^{+38}–W^{+73}. However it is notes that the strongest lines of a stage may be in other spectral regions, particularly the VUV. Figure 6.2 shows the distribution of the contributing ionisation stages.

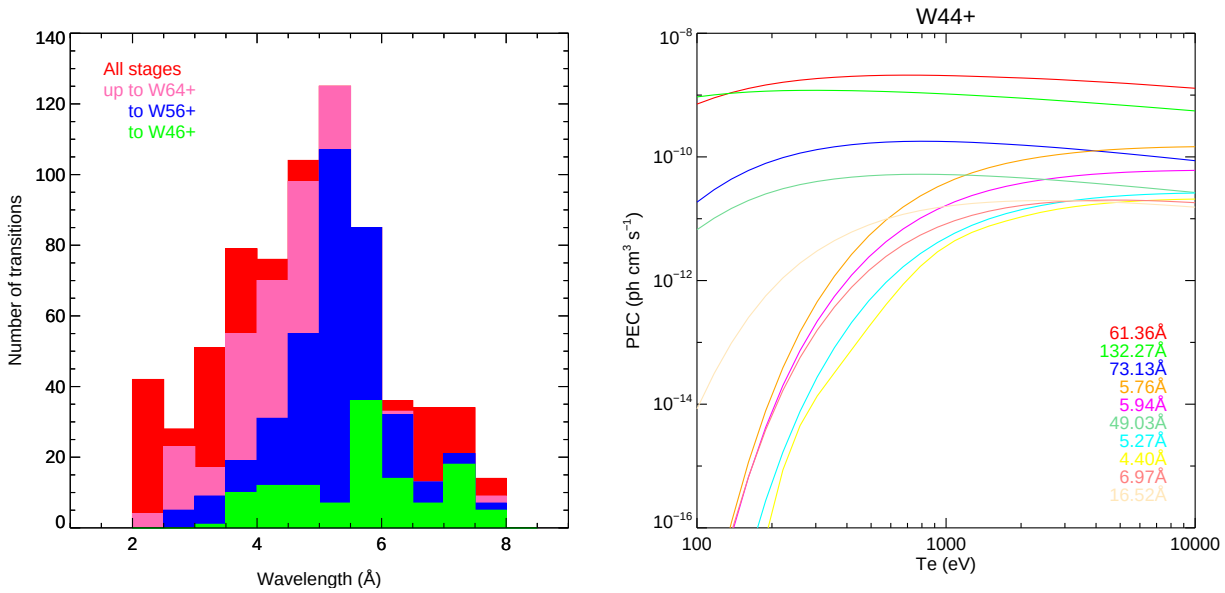

Figure 6.2: (left) Ionisation stage origin of X-ray lines. (right) PECs of W^{+44} predicted to be the dominant stage in the UP X-ray system.

The distribution of stages and predicted spectra for the chords in figure 6.1 is shown in figure 6.2.

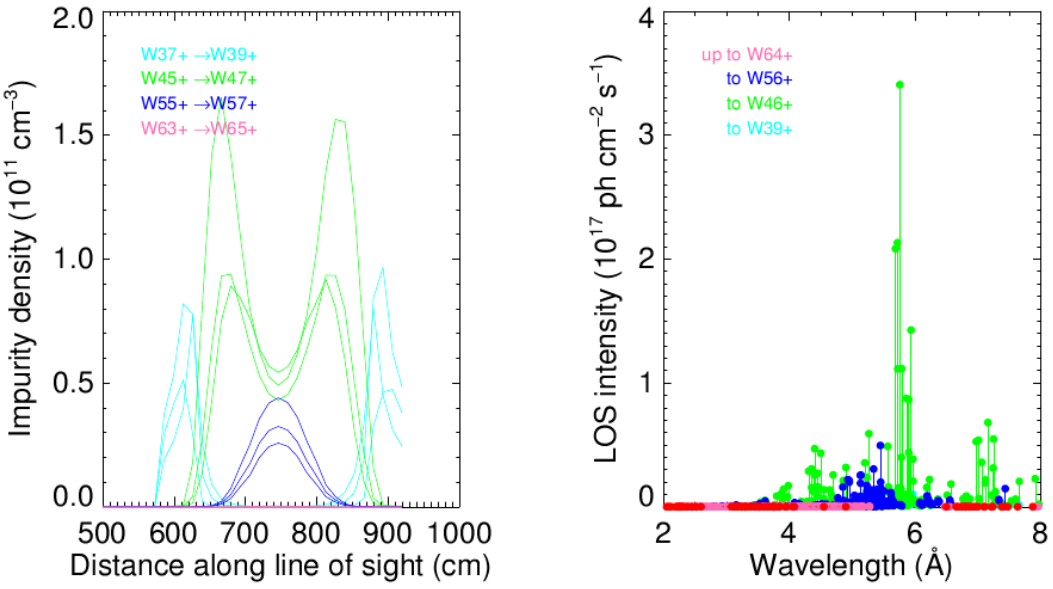

Figure 6.3: Fractional abundance of tungsten along one of the possible LOS.

The predicted spectrum will change depending on the chord but the strongest line across all chords is the W^{+44} line at 5.7580Å arising from the $3d^{10}\ 4s^2\ {}^1S_0 - 3d^9\ 4s^2\ 4f\ {}^1P_1$ transition. The integrated emissivity of this emission line as a function of LOS is shown in figure 6.2.

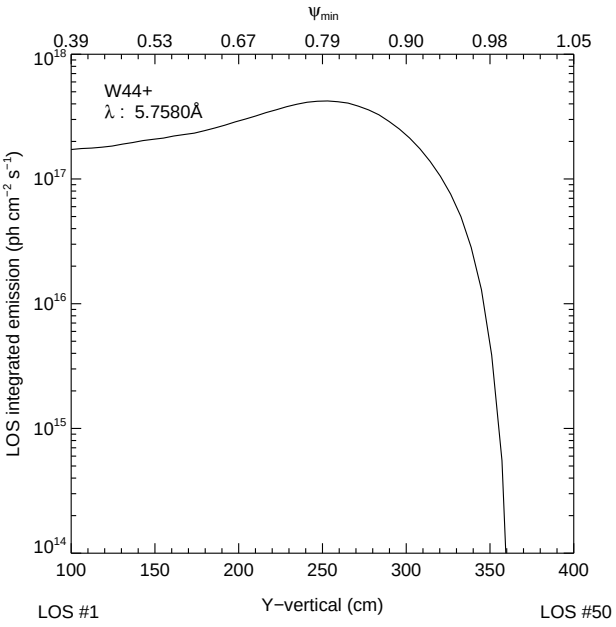

Figure 6.4: W^{+44} line at 5.7580Å mapped against vertical intercept of chord and minimum flux label.

The edge conditions of ITER correspond to those in the core of many present day machines so a number of the X-ray lines have been observed. Table 6.2 catalogues the strongest for a number of ionisation stages.

Pubs: A E Kramida and T Shirai, Atomic Data Nuclear Data Tables, 95 (2009) p305-474
T Peutterich et al, PPCF, 50 (2008) 085016
R Neu, 'Tungsten as a Plasma Facing Material in Fusion Devices', (2003) IPP10/25
PEC, wavelength from ADAS adf15 dataset

stage	wavelength			transition				source
	PEC	Pub.	Neu					
38	4.70577		4.71	3dA 4s2 4p6	(1)0(0.0) -	3d9 4s2 4p6 5f1	(1)1(1.0)	
38	4.81449		4.83	3dA 4s2 4p6	(1)0(0.0) -	3d9 4s2 4p6 5f1	(3)2(1.0)	
38	5.46763			3dA 4s2 4p6	(1)0(0.0) -	3dA 4s2 4p6 4d1	(1)1(1.0)	
38	5.96454			3dA 4s2 4p6	(1)0(0.0) -	3d9 4s2 4p6 4f1	(1)1(1.0)	
38	6.15374			3dA 4s2 4p6	(1)0(0.0) -	3d9 4s2 4p6 4f1	(3)2(1.0)	
38	6.86168			3dA 4s2 4p6	(1)0(0.0) -	3d9 4s2 4p6 4d1	(1)2(2.0)	
38	7.33339			3dA 4s2 4p5 4d1	(3)2(1.0) -	3d9 4s2 4p6 4d1	(1)0(0.0)	
38	7.65507		7.64	3dA 4s2 4p5 4d1	(1)1(1.0) -	3d9 4s2 4p6 4d1	(1)0(0.0)	
39	5.92268			3dA 4s2 4p5	(2)1(1.5) -	3d9 4s2 4p5 4f1	(2)1(1.5)	
39	5.92657			3dA 4s2 4p5	(2)1(1.5) -	3d9 4s2 4p5 4f1	(2)2(2.5)	
39	5.92927			3dA 4s2 4p5	(2)1(1.5) -	3d9 4s2 4p5 4f1	(2)0(0.5)	
39	6.10836			3dA 4s2 4p5	(2)1(1.5) -	3d9 4s2 4p5 4f1	(4)2(1.5)	
39	6.11526			3dA 4s2 4p5	(2)1(1.5) -	3d9 4s2 4p5 4f1	(2)2(2.5)	
39	7.52952	7.560	7.57	3dA 4s2 4p5	(2)1(1.5) -	3d9 4s2 4p6	(2)2(2.5)	Kramida
40	5.88734	5.8929	5.89	3dA 4s2 4p4	(3)1(2.0) -	3d9 4s2 4p4 4f1	(3)2(3.0)	Kramida
40	5.88749	"		3dA 4s2 4p4	(3)1(2.0) -	3d9 4s2 4p4 4f1	(3)1(2.0)	Kramida
40	6.07577		6.08	3dA 4s2 4p4	(3)1(2.0) -	3d9 4s2 4p4 4f1	(1)3(3.0)	
40	7.45938	7.490	7.48	3dA 4s2 4p4	(3)1(2.0) -	3d9 4s2 4p5	(3)2(3.0)	Kramida
41	5.85328		5.83	3dA 4s2 4p3	(2)2(1.5) -	3d9 4s2 4p3 4f1	(2)3(2.5)	
41	5.85726			3dA 4s2 4p3	(2)2(1.5) -	3d9 4s2 4p3 4f1	(4)1(1.5)	
41	6.03954		6.04	3dA 4s2 4p3	(2)2(1.5) -	3d9 4s2 4p3 4f1	(2)2(2.5)	
41	7.39442	7.410	7.41	3dA 4s2 4p3	(2)2(1.5) -	3d9 4s2 4p4	(2)1(1.5)	Kramida
41	7.39566	"		3dA 4s2 4p3	(2)2(1.5) -	3d9 4s2 4p4	(2)2(2.5)	Kramida
42	7.33088	7.340	7.32	3dA 4s2 4p2	(3)1(0.0) -	3d9 4s2 4p3	(3)0(1.0)	Kramida
43	5.78289	5.7928	5.79	3dA 4s2 4p1	(2)1(0.5) -	3d9 4s2 4p1 4f1	(2)1(0.5)	Kramida
43	5.78761	5.7951		3dA 4s2 4p1	(2)1(0.5) -	3d9 4s2 4p1 4f1	(2)2(1.5)	Kramida
43	5.96863	5.98	5.98	3dA 4s2 4p1	(2)1(0.5) -	3d9 4s2 4p1 4f1	(2)1(1.5)	Puetterich
43	5.96894	5.98		3dA 4s2 4p1	(2)1(0.5) -	3d9 4s2 4p1 4f1	(4)2(0.5)	Puetterich
44	4.40311	4.411		3dA 4s2	(1)0(0.0) -	3d9 4s2 5f1	(1)1(1.0)	Kramida
44	4.49947	4.507	4.49	3dA 4s2	(1)0(0.0) -	3d9 4s2 5f1	(3)2(1.0)	Kramida
44	4.69757			3dA 4s2	(1)0(0.0) -	3p5 3dA 4s2 4d1	(3)2(1.0)	
44	4.89961			3dA 4s2	(1)0(0.0) -	3p5 3dA 4s2 4f1	(1)2(2.0)	
44	5.26610		5.26	3dA 4s2	(1)0(0.0) -	3p5 3dA 4s2 4d1	(1)1(1.0)	
44	5.75796	5.75	5.75	3dA 4s2	(1)0(0.0) -	3d9 4s2 4f1	(1)1(1.0)	Puetterich
44	5.93571	5.95	5.95	3dA 4s2	(1)0(0.0) -	3d9 4s2 4f1	(3)2(1.0)	Puetterich
44	6.97155			3dA 4s1 4p1	(1)1(1.0) -	3d9 4s2 4d1	(1)0(0.0)	
45	5.72088	5.7192		3dA 4s1	(2)0(0.5) -	3d9 4s1 4f1	(2)1(1.5)	Kramida
45	5.72416	5.7240		3dA 4s1	(2)0(0.5) -	3d9 4s1 4f1	(2)1(0.5)	Kramida
45	5.89862	5.9127	5.91	3dA 4s1	(2)0(0.5) -	3d9 4s1 4f1	(4)2(1.5)	Kramida
45	5.89931	"		3dA 4s1	(2)0(0.5) -	3d9 4s1 4f1	(4)2(0.5)	Kramida
45	7.05857	7.075	7.07	3dA 4s1	(2)0(0.5) -	3d9 4s1 4p1	(2)1(1.5)	Kramida
45	7.24593	7.242	7.25	3dA 4s1	(2)0(0.5) -	3d9 4s1 4p1	(2)1(1.5)	Kramida
46	5.68748	5.6900	5.69	3dA	(1)0(0.0) -	3d9 4f1	(1)1(1.0)	Kramida
46	5.86308	5.8665	5.87	3dA	(1)0(0.0) -	3d9 4f1	(3)2(1.0)	Kramida
46	7.00977	7.02	7.02	3dA	(1)0(0.0) -	3d9 4p1	(1)1(1.0)	Puetterich
46	7.15892	7.16	7.16	3dA	(1)0(0.0) -	3d9 4p1	(3)2(1.0)	Puetterich
46	7.90963	7.93	7.93	3dA	(1)0(0.0) -	3d9 4s1	(1)2(2.0)	Puetterich
47	5.56441	5.5686	5.56	3d9	(2)2(2.5) -	3d8 4f1	(2)3(3.5)	Kramida
48	5.44834	5.4522	5.45	3d8	(3)3(4.0) -	3d7 4f1	(3)4(5.0)	Kramida
53	4.93100			3d3	(4)3(1.5) -	3d2 4f1	(4)4(2.5)	
53	4.95226			3d3	(4)3(1.5) -	3d2 4f1	(4)4(2.5)	
53	4.95234			3d3	(4)3(1.5) -	3d2 4f1	(4)3(1.5)	
54	4.85071			3d2	(3)3(2.0) -	3d1 4f1	(3)4(3.0)	
55	4.77240			3d1	(2)2(1.5) -	4f1	(2)3(2.5)	
60	3.79254			3s2 3p2	(3)1(0.0) -	3s2 3p1 4d1	(3)2(1.0)	
60	4.47316			3s2 3p1 3d1	(3)2(1.0) -	3s2 3p1 4f1	(3)2(2.0)	

Table 6.1: The strongest predicted lines of tungsten in the X-ray region.

Chapter 7

H-α (and visible spectroscopy) viewing system

7.1 Instrument

The primary role of this diagnostic is to measure line emission of hydrogen isotopes and impurities from ITER First Wall. There are a number of cameras to cover the full poloidal extent and there is a toroidal component to the view.

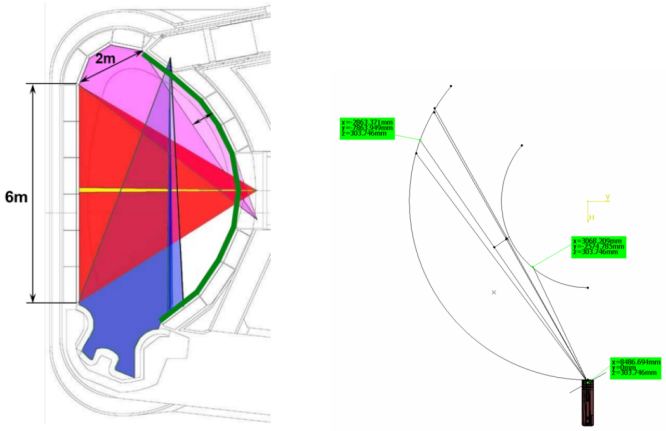

Influx measurements are location specific as seen in figure 7.1 so as full a poloidal coverage as possible is required.

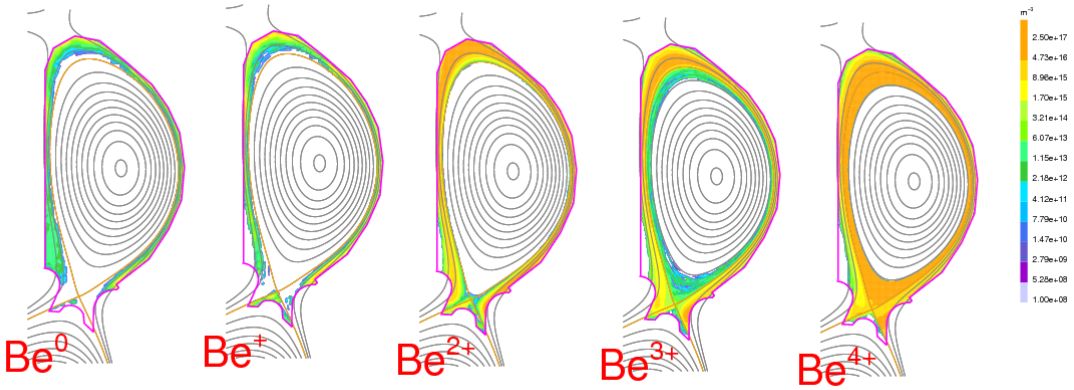

Figure 7.1: The variation in poloidal extent of Be ionisation stages (0.4% concentration).

7.2 Fuel and impurity emission

The ionisation per photon coefficient relates the local intensity to a particle flux:

$$\Gamma = \mathcal{SXB}_{j\to k} \int \varepsilon_{j\to k}(\zeta)\, d\zeta = \mathcal{SXB}_{j\to k} I_{j\to k}$$

The instrument is optimized to measure H- α emission at 6562Å but the spectrometers can measure down to ~4000Åwith a transmission loss of a factor of 2 loss in the silica fibres. Transitions for a number of influx elements occur in this region and their SXB and PEC coefficients are compared in table 7.2.

	λ (nm)	PEC (ph cm^{3}s^{-1})	SXB
H-α	656	2.35×10^{-9}	11.54
BeII	527	3.78×10^{-10}	33.41
H-β	486	5.27×10^{-10}	51.44
CIII	465	1.48×10^{-9}	1.34
BeI	457.3	5.36×10^{-9}	15.04
OII	441.9	5.66×10^{-10}	17.64
WI	400.8	4.00×10^{-10}	96.7

Table 7.1: Ranking of photon emissivity and ionisation per photon coefficients (at 40eV and 10^{18}m^{-3}) for probable visible lines. Note that the neutral tungsten values are subject to revision.

To maximize the emission the design incorporated a toroidal component to the viewing angle. Figure 7.2 shows the enhancement over a purely poloidal view.

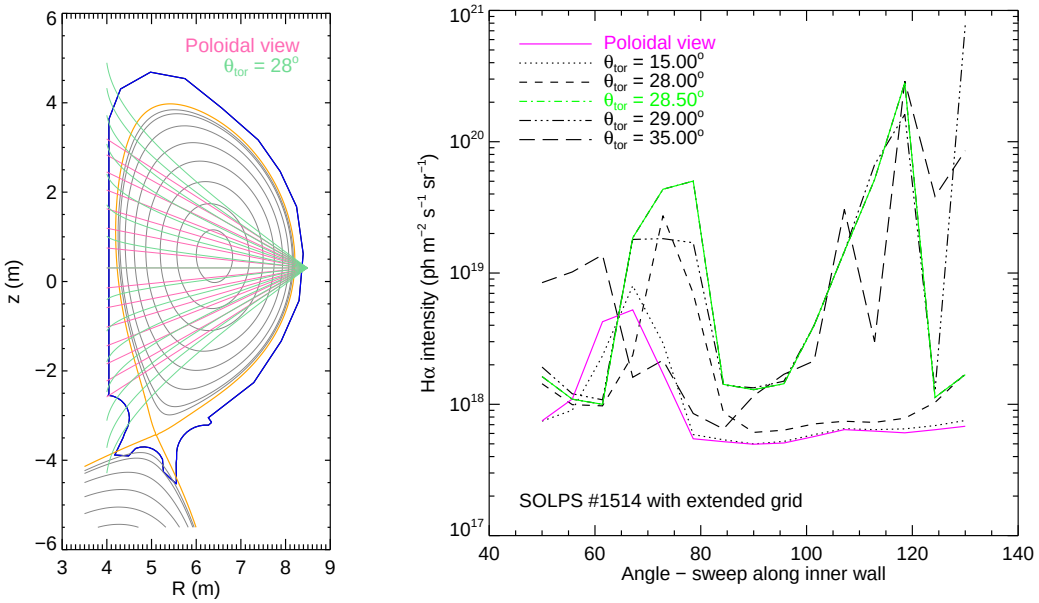

Figure 7.2: (left) Lines of sight for model emission showing the extended length of those with a toroidal component. (right) H- α emission along the inner wall for a set of tangential views.

A toroidal component also improves the signal strength of key BeI and BeII lines as show in figure 7.2.

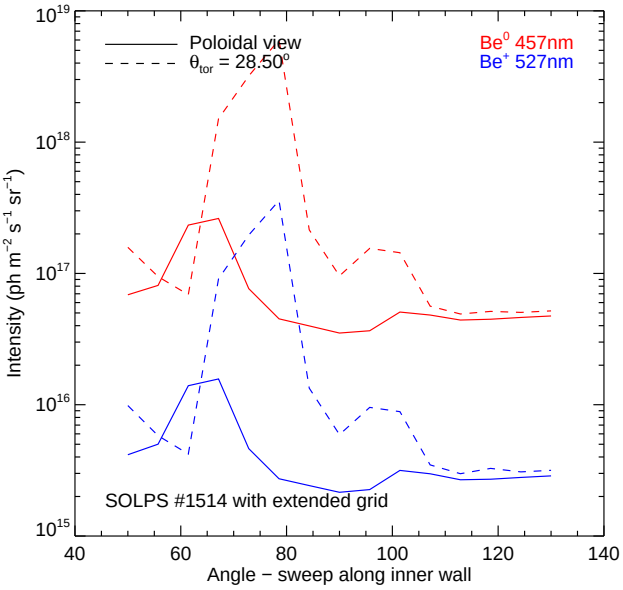

Figure 7.3: The intensity of BeI and BeII along the inner wall.

Chapter 8

Radial soft X-ray camera

The radial soft X-ray system is a set of cameras which view a poloidal cross section of ITER. The initial baseline system will use conventional pin-diode detectors and is similar to existing systems on present day machines. The radiated power coefficients required for emission modelling must incorporate the energy response of the detector.

8.1 Calculation of soft X-ray radiated power coefficients

The total radiated power is a combination of discrete line radiation and continuum emission. The *adf11* coefficients do not have an energy or wavelength dependence. When modelling SXR emission we need to use modified coefficients which take account of the energy dependence of the response of the detector and the energy cutoff nature of any window. The SXR filter is a transmission fraction (0–1) as a function of energy, $f(E)$. For line emission

$$P_{sxr}^{line} = \sum f(E) P_i(E)$$

The P_{sxr} coefficient can be calculated as part of a collisional-radiative calculation or by summing a set of photon emissivity coefficients.

The continuum emission comprises 3 parts, radiative recombination, dielectronic recombination and bremsstrahlung. Radiative recombination is assumed to release energy equal to ground state ionisation energy of the recombined ion. Dielectronic recombination energy loss is summed over the two parent transitions and each is assumed to release an energy equal to the parent transition energy together with the ionisation energy of the ground state of the recombined ion. Bremsstrahlung is taken to be hydrogenic with free-free Gaunt factor set to unity.

$$P_{sxr}^{rb} = 1.6 \times 10^{-19} \left\{ \alpha_r^{(z+1 \to z)} \chi + \sum_{j=1}^{2} \left[\alpha_r^{(z+1 \to z)} (\Delta E_j + \chi) \right] \right\} + 1.54 \times 10^{-32} z_i^2 g_{\mathrm{ff}} \sqrt{(kT_e / I_H)} \qquad (\mathrm{Wcm}^3)$$

The SXR *adf11* coefficients incorporate the filter function thus:

$$P_{sxr}^{BR} = 1.54 \times 10^{-32} z_i^2 g_{\mathrm{ff}} \int_0^{\infty} f(E) \exp(-E/kT_e)\, dE$$

$$P_{sxr}^{DR} = 1.6 \times 10^{-19} \sum \alpha_{DR} \left[f(\chi)\chi + f(\Delta E)\Delta E_j \right]$$

$$P_{sxr}^{RR} = 2.6 \times 10^{-14} T_e \qquad \Big((I_h/T_e)^{1/2} \frac{z^2(2n^2 - \mu)}{n^3} \chi \int_{\chi}^{\infty} f(E) + (I_H/kT_e)^{3/2} \sum_{j=n+1}^{N_G} \frac{2z^4}{j^3} \int_{I_h z^2/n^2 T_e}^{\infty} f(E) \exp(-E/kT_e)\, dE \Big)$$

It is not possible to apply a simple filter post-process to the total radiated power coefficients to model SXR radiation.

8.2 Diode response

The response of a diode similar to the one used at JET and of the same family as the proposed ITER system, a Centronic LD20-5T with 20 on-chip channels was measured by Cho [4]. The important detail is that the measured characterization is markedly different from standard theory. The Cho model, which includes diffusion effects in addition to the depletion layer and substrate size effects, is found to have the best match to the measurements. The diodes in [4] were operated with a 1V bias whereas there is a 3V bias voltage in the normal JET operation. Note that there is a difference of 20% (at an energy of 5keV) between diodes biased at 1.3V and 6V [5]. A fit to the Cho model using the ADAS model gives an 'effective' depth of 38.8μm with an over-estimation at the peak of 10%. The response of the diode, will change depending on the neutron flux it subject to. The figure from [5] exposed the JET diodes to fluxes of 10^{13}, 2×10^{13} and 1.5×10^{14}neutrons cm^{-2}.

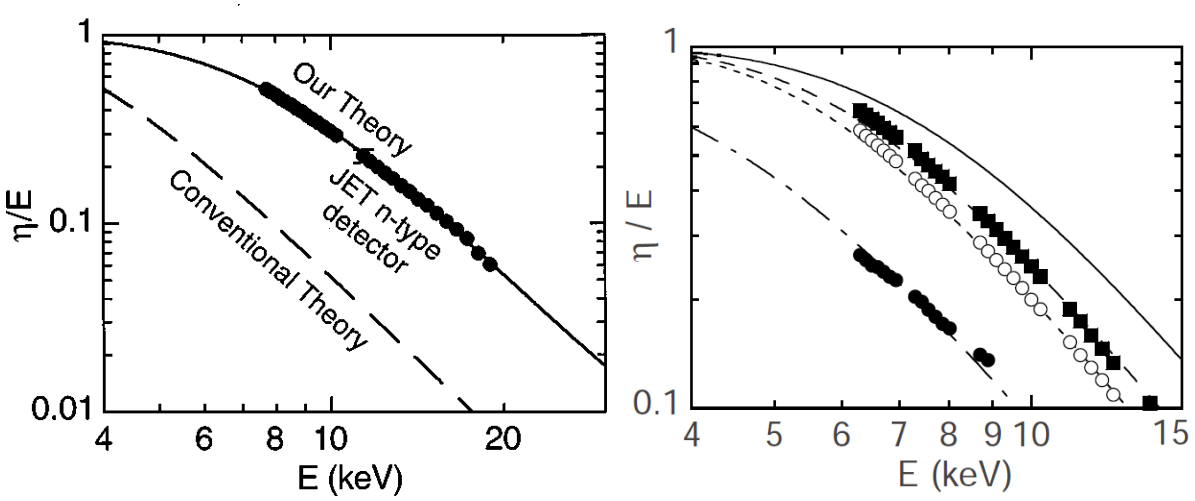

Figure 8.1: (left) Transmission fraction of diodes, similar to JET units, measured by T. Cho (figure 1 in [4]). (right) X-ray response to neutron fluence, figure 2 of [5]. Full line — no flux, squares 10^{13}, open circles 2×10^{13} and filled circles 1.5×10^{14}neutronscm^{-2}.

For the SXR system for the ITER radial X-ray camera consider a 100μm Be window, a 5μm Mylar protection and a Cho-like diode response. The convolution of these elements is the SXR filter function and is shown in figure 8.2. Note that the diode response is the least precise component of the filter and therefore the energy response was taken from a digitization of the Cho figure.

8.3 Line emission through the SXR window

Each transition occurs at an energy determined by the atomic structure of the ionisation stage. It is possible to represent the total line emission of a stage by a limited number of effective lines. The shift in energy between these representative transitions and the transitions which compose is small compared to the energy window of the SXR filter. These energies are drawn from ADAS *adf03* datasets and are overlaid with the ITER filter in figure 8.3.

The Be window cuts-off most of the line emission from the light elements, with a notable exception being the He-like and H-like stages of Argon. The He-like and H-like stages of iron, and the other mid-Z elements, lie on the falling part of the curve which demands that the high energy cutoff is an important parameter. Although much of the line emission from tungsten is blocked lines from a wide range of stages, W^{+38} – W^{+70}, fall within the transparency window of the soft X-ray filter.

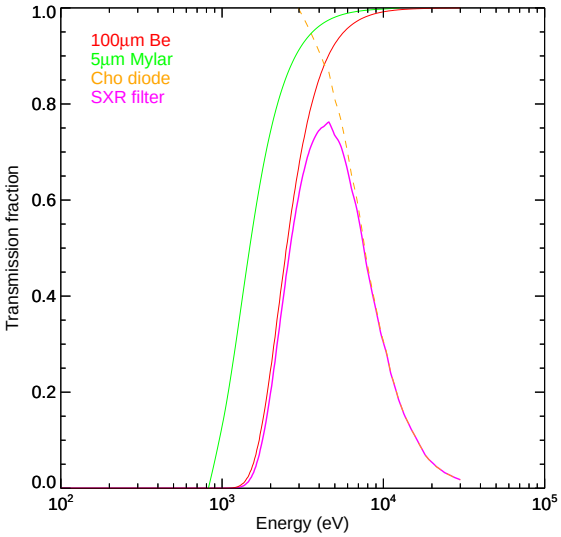

Figure 8.2: SXR filter, and its components, used for ITER predictions.

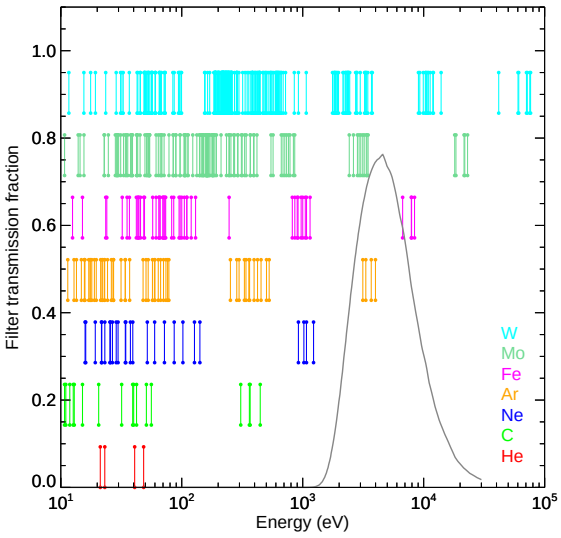

Figure 8.3: Energies of the 'effective' emission lines of various ITER relevant elements.

Consider argon, in which both line and continuum emission fall in the transparent energy range of the SXR filter. The difference in the admitted radiation of the various filters and the effect of neutron fluence is shown in figure 8.4. The differences are notable but, although important for interpretation of the results, is not great enough to affect the design of the instrument.

8.4 Impurity mix

Distinguishing individual elements with a broad coverage SXR system is challenging. Such measurements are possible when an influx event raises the contribution of an impurity above the background signal level. SXR emission following laser ablation or gas puffing has been successfully used for profile measurements in impurity transport experiments.

The routine measurements of the system will be of an impurity mix representative of quiescent operation. To compare the different scenarios we choose to fix the individual impurity concentration ($n_{\rm imp}/n_e$) and consider mixtures

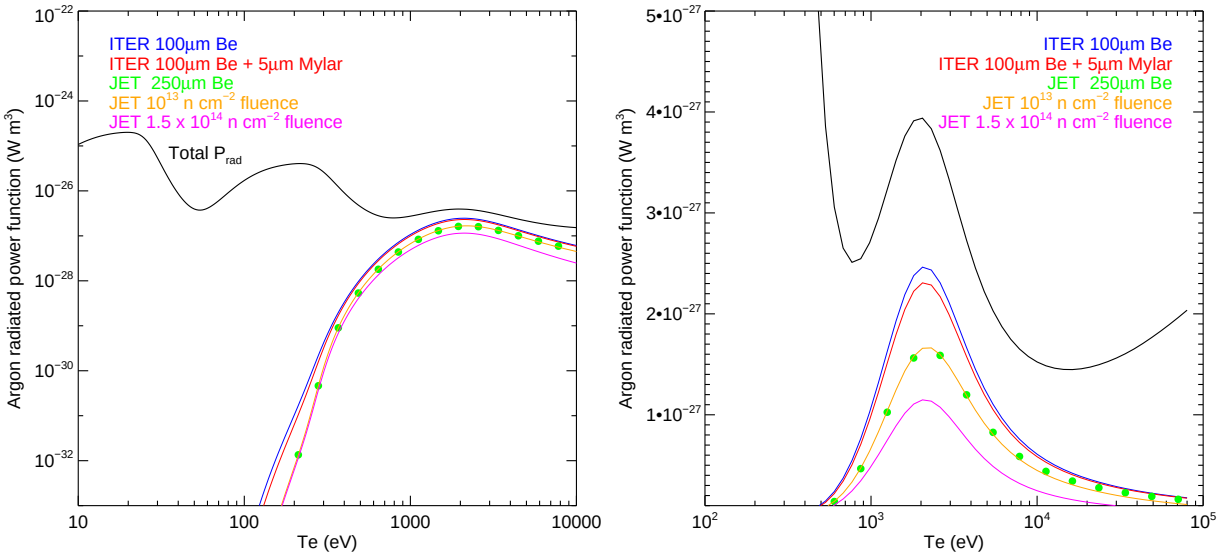

Figure 8.4: SXR emission seen by various JET and ITER-proposed SXR filters.

of elements representative of early plasma operation and those with added control gases. See table 8.1.

	Impurity mix
Early-phase plasma	3% Be, 0.01% Fe, 0.0001% W
Radiating edge	2% He, 2% Be, 0.01% Fe, 0.0001% W, 0.12% Ar

Table 8.1: Representative impurity mixes for early phase operation and control gas operations.

Table 8.2 details the volume integrated total radiated power and soft X-ray power for a 1% concentration of each impurity. Note that, particularly for the deliberately introduced control gases, radiation from the edge can be of the same order as the core contribution but the SANCO edge model does not have a good model of the plasma edge and has been omitted in the table.

	P_{rad} and P_{sxr} /MW							
	1% He		1% Be		1% C		1% N	
15MA inductive burn	0.52	0.06	2.60	0.04	7.04	0.75	10.43	0.76
7.5MA H-mode	0.10	0.01	0.50	0.00	1.37	0.12	2.07	0.11
10MA H-mode ramp-up	0.21	0.02	1.05	0.02	2.90	0.30	4.36	0.30
10MA H-mode ramp-down	0.15	0.02	0.76	0.01	2.05	0.23	3.04	0.24
10MA L-mode ramp-up	0.02	0.00	0.10	0.00	0.37	0.01	0.69	0.01
15MA QDT=10 flat density profile	0.53	0.06	2.63	0.04	7.10	0.75	10.49	0.76
15MA QDT=10 peaked density profile	0.43	0.05	2.13	0.04	5.70	0.69	8.32	0.72

	P_{rad} and P_{sxr} /MW					
	1% Ar		1% Fe		1% W	
15MA inductive burn	173.39	60.22	647.20	236.14	8437.66	1601.54
7.5MA H-mode	39.85	14.69	146.78	53.57	1989.06	347.00
10MA H-mode ramp-up	76.20	25.20	263.58	86.01	3552.07	589.49
10MA H-mode ramp-down	46.42	14.95	170.86	58.00	2074.18	407.42
10MA L-mode ramp-up	16.44	3.18	47.49	6.94	586.25	43.56
15MA QDT=10 flat density profile	170.05	59.05	662.55	250.35	8222.05	1682.02
15MA QDT=10 peaked density profile	109.60	33.03	447.90	161.43	4715.24	1135.66

Table 8.2: 1% contributions to total and filtered SXR power.

8.5 Radiated power and soft X-ray profiles

Emission from an impurity mix I: 3% Be, 10^{-4} Fe, 10^{-6} W, Z_{eff} = 1.43

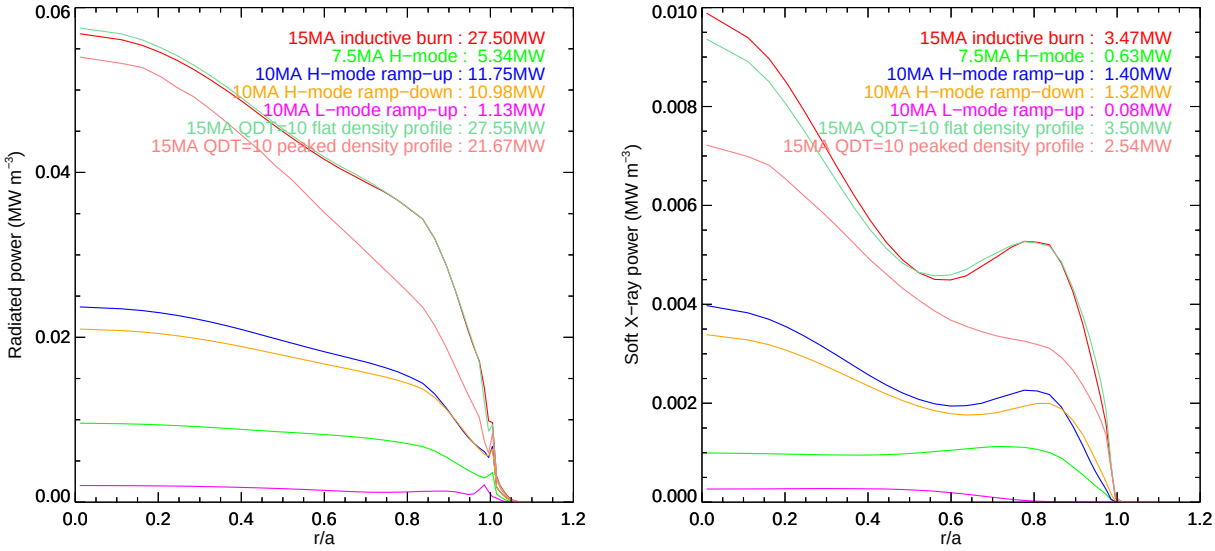

Figure 8.5: Total radiated power and soft X-ray power for a number of ITER scenarios with an impurity mix representative of early phase operation.

Emission from an impurity mix II: 2% He, 2% Be, 10^{-4} Fe, 10^{-6} W, 0.12% Ar, Z_{eff} = 1.72

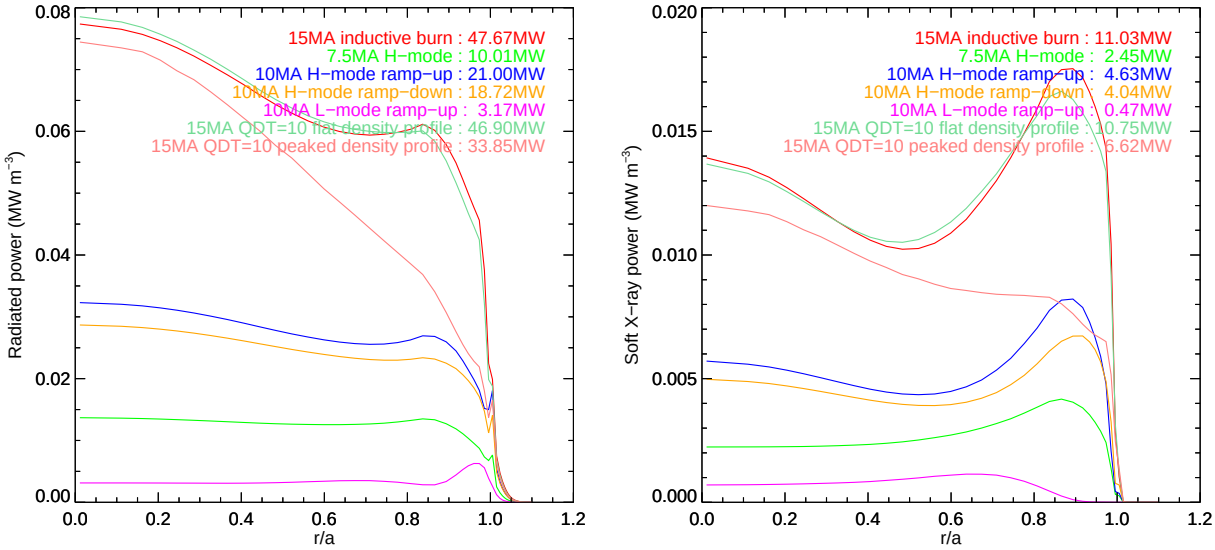

Figure 8.6: Total radiated power and soft X-ray power for a number of ITER scenarios with an impurity mix representative of early phase operation.

8.6 Total and Soft X-ray breakdown by element

The local conditions, and to a lesser extent the transport, determines the radial location of the radiated power. The contribution of each element to the total will change depending on the plasma scenario. Plotting normalized elemental soft X-ray contributions shows the potential for distinguishing between different impurities in a measurement.

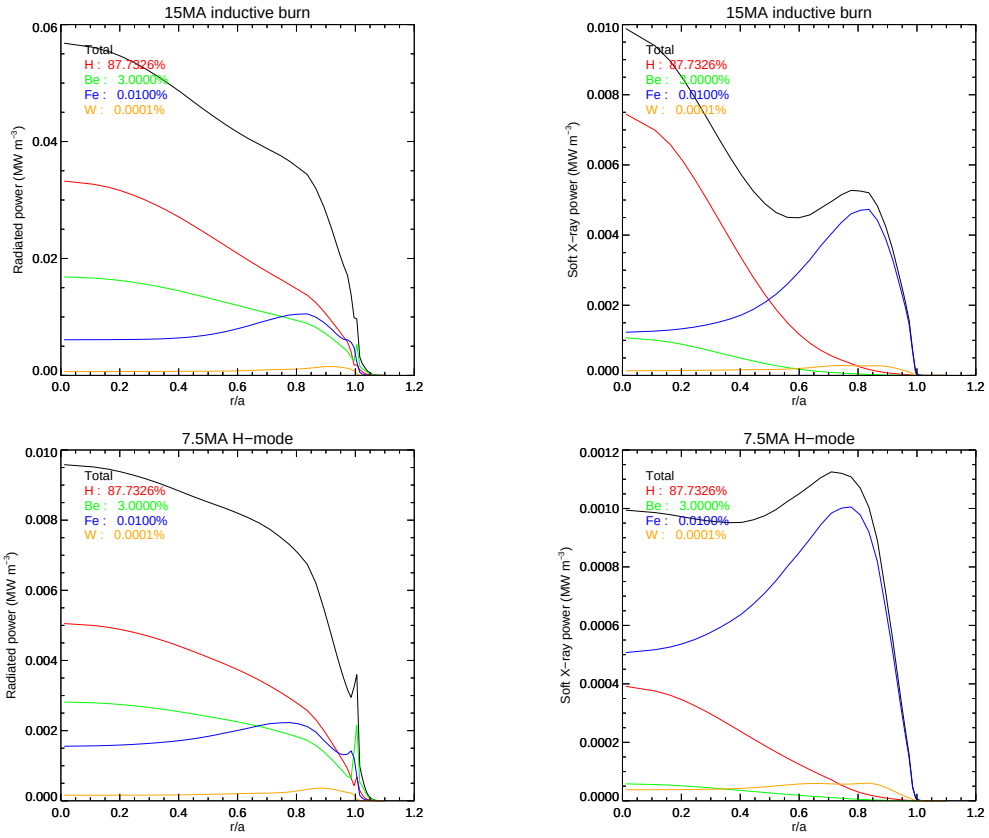

Figure 8.7: Contribution of each impurity to total and soft X-ray radiated power for a high and low temperature ITER plasma.

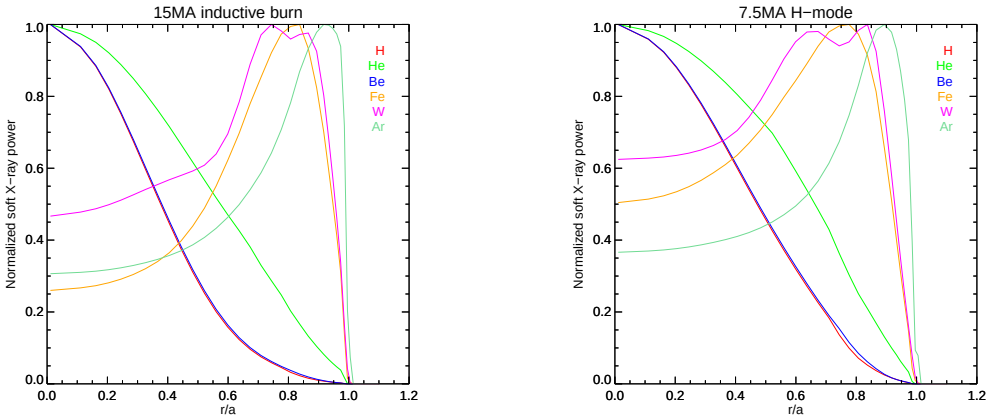

Figure 8.8: Normalized contribution of each impurity to total and soft X-ray radiated power for a high and low temperature ITER plasma.

8.7 Response of soft X-ray emission to a sawtooth crash and ELMs

The radial SXR diagnostic must respond to transient plasma events, of which ELMs and sawteeth are the most common. Sawteeth are a core MHD phenomenon related to the $q = 1$ surface while ELMs are manifested in the outer edge region of the plasma.

The simplest sawtooth model is one where the temperature profile suddenly flattens and then relaxes back to its pre-crash shape. The relaxation time is taken as 20s and electron density and impurity transport are not assumed to change throughout the event. The pre and post electron temperature profiles, shown in figure 8.9 are supplied by the ITER physics group.

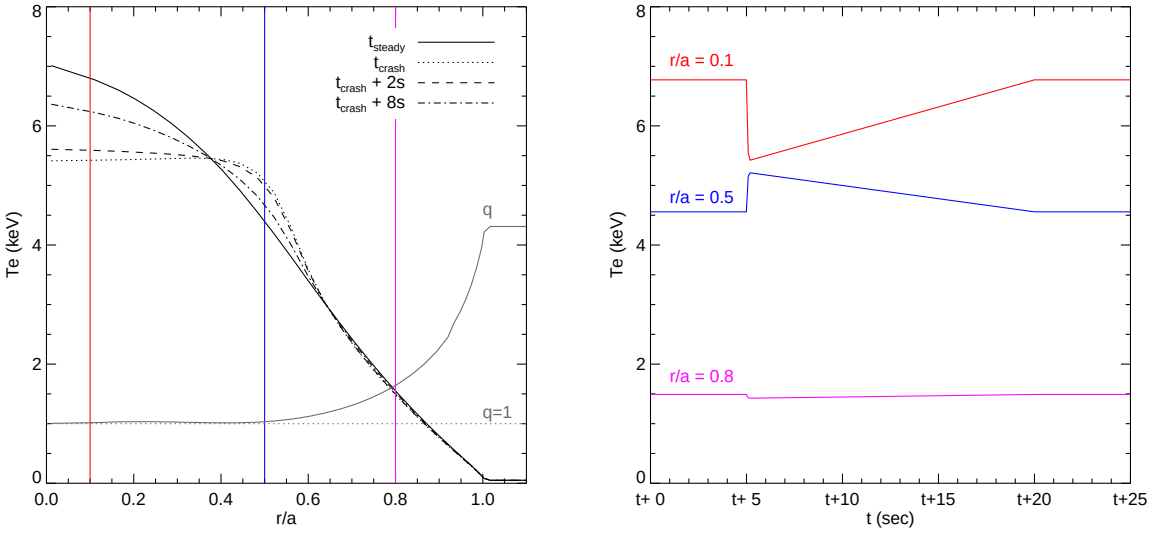

Figure 8.9: (left) Temperature profile before and during sawtooth crash. (right) Selected temporal slices.

Figure 8.10 shows that a clear signal is seen in the soft X-ray emission.

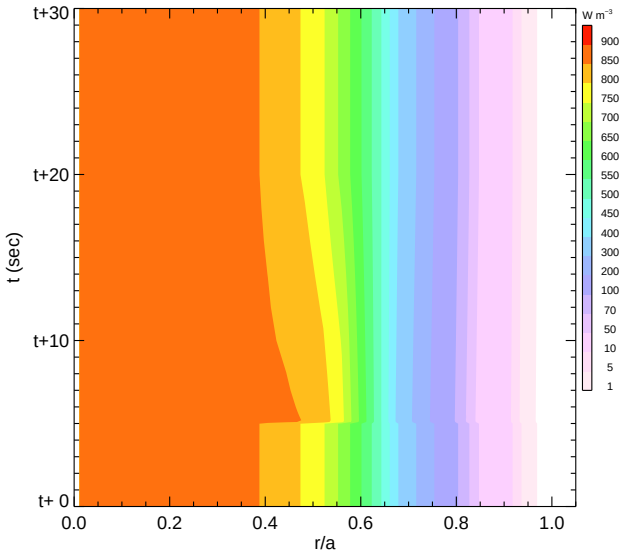

Figure 8.10: Perturbation to impurity mix I caused by a sawtooth crash.

ELMs come in two flavours, controlled and uncontrolled. We note that the reference operating scenarios of ITER preclude ELMs because of the disruption risk they pose although the controlled ones may be acceptable. The model used here is one where the density profiles in a fixed area are modified. For the uncontrolled ELMs the electron temperature profile is changed also.

The ELM crash is of the order of 250μs and the recovery to pre-ELM conditions is expected to be 0.5–1sec. The frequency of the controlled ELMs is 3—60Hz, corresponding to a profile recovery time of 0.017–0.035 sec. Figure 8.11 shows the extend of the profile modification.

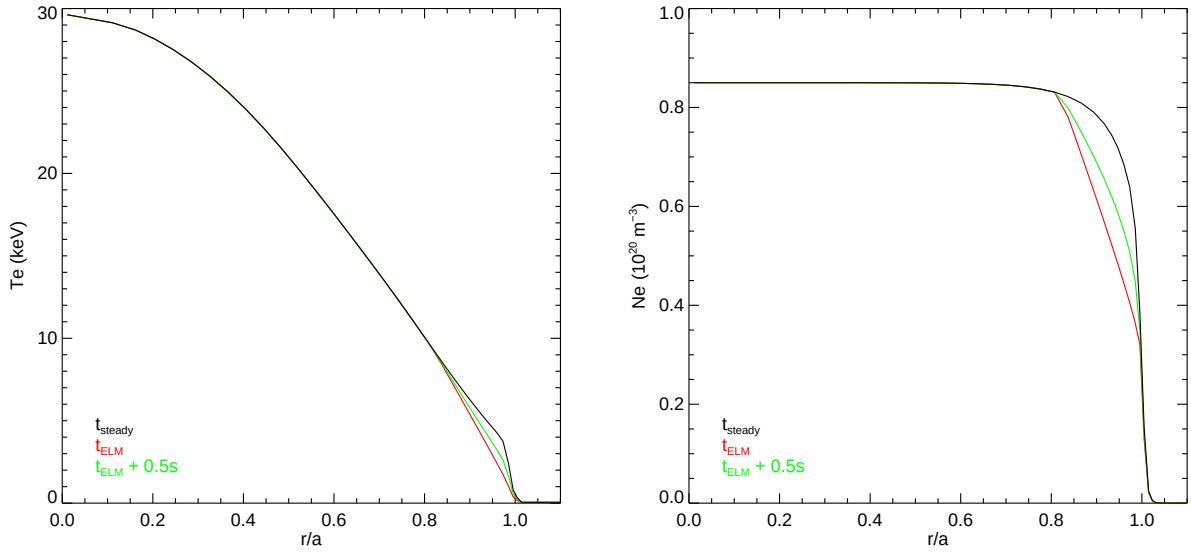

Figure 8.11: Temperature and density profiles before and after the ELM.

The uncontrolled ELM will be measurable with the SXR instrument as seen in figure 8.12.

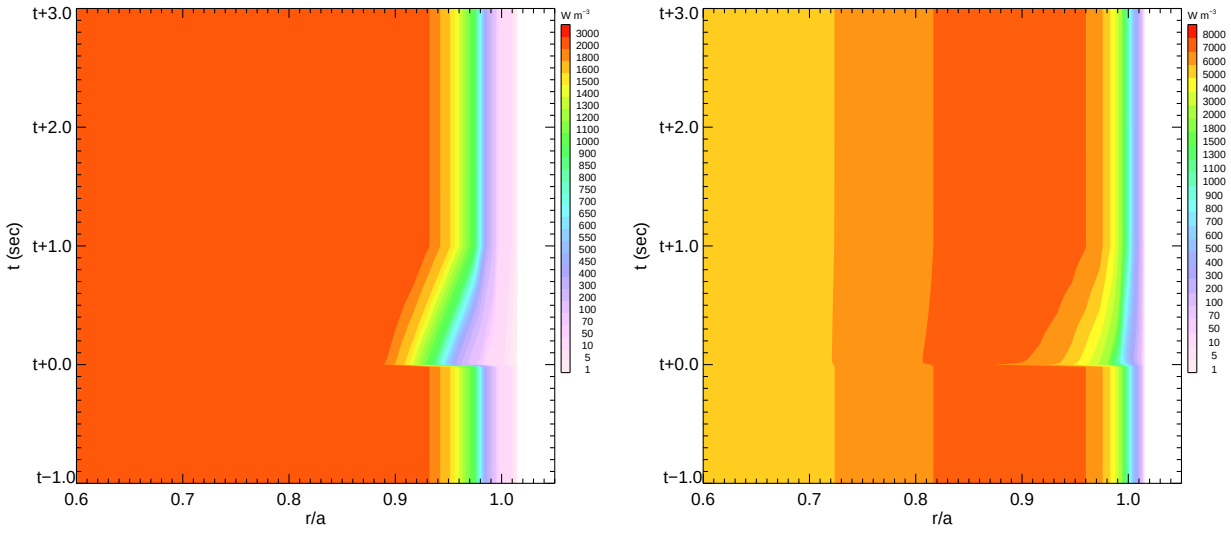

Figure 8.12: Perturbation to impurity mix I and II caused by an uncontrolled ELM.

The recovery time of the profiles in the controlled case are of the same order as the transport time so the time response of the signal may be smoothed. However the emission predictions indicate that the signal will be usable as a

diagnostic as seen in figure 8.13.

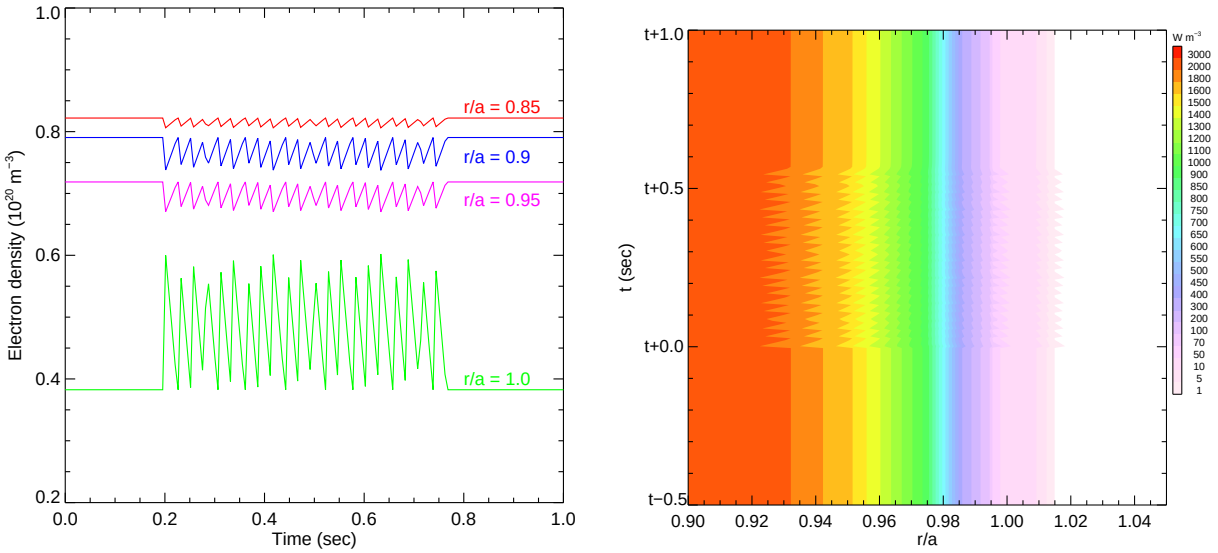

Figure 8.13: (left) Variation in electron density across the ELM footprint. (right) Response of SXR system to controlled ELMs for the early phase impurity mix.

Chapter 9

Radiated power calculations

Radiated power produced by impurities is a concern for the operation of ITER. Usually it is a property to be minimized but occasionally the power radiated can be used to ameliorate more deleterious effects by quenching the plasma. Accurate atomic data is required, some of which have not been available previously in ADAS.

9.1 Radiated power from Cadmium

There is a potential for a cadmium influx into the vacuum due to the generation and outgassing of cadmium transmuted in the silver wire used for welding in magnetic coil diagnostics. The number of Cd atoms released over the lifetime of ITER can be estimated from the exposed area and transmutation rate. Estimating the contribution to radiated power required *adf11* data from ADAS. The heavy species machinery (publication 3 of ADAS-EU) allowed the rapid production of these data.

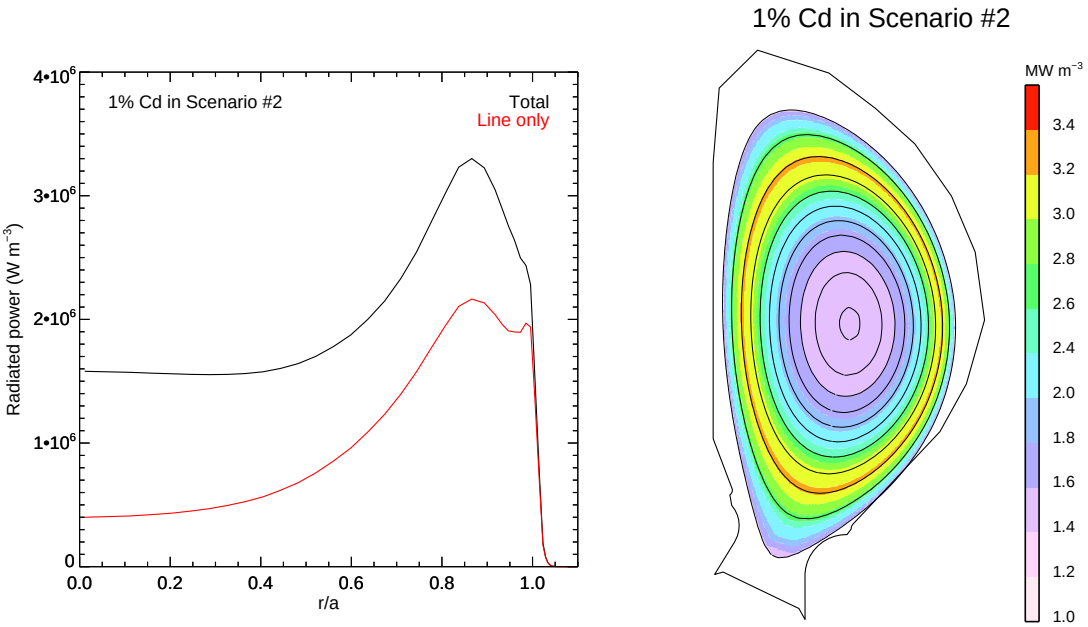

Figure 9.1: The radiated power and distribution of 1% Cd in an ITER reference plasma. The radiated power can be easily scaled to the actual concentration.

Cd will add 2kW of extra radiated power. Not unexpectedly the conclusion is that this is insignificant when impurities are expected to contribute 10MW.

9.2 Response of bolometer to radiated power

Preliminary calculations for modelling the bolometer system have been undertaken. A concern is the response at high temperatures due to absorption in the gold coating. Figure 9.2 shows the departure from the total radiated power from its equilibrium value for iron. There is a slight underestimation at low temperatures due to reflection and the absorption effect is seen in the iron continuum radiation but is only significant for electron temperatures well above those expected for ITER operations.

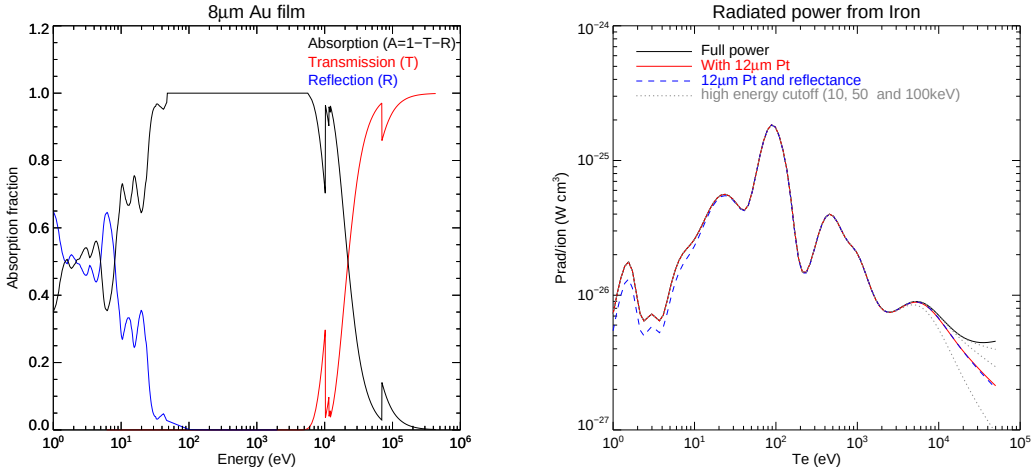

Figure 9.2: (left) Absorption curve for ITER bolometer. (right) Radiated power from iron seen by various ITER bolometer proposals compared to simple high energy cut-off.

9.3 Time evolution of impurities in FPSS system

The Fusion Power Shutdown System FPSS is a safety system designed to terminate the the plasma in the case of loss of coolant accident in the divertor. Gas is introduced on a relatively slow timescales to ensure the dissipation of sufficient stored energy in order to extinguish the burning plasma (350 MJ). The simplest estimation of the amount of gas required is to calculate the energy radiated per ion in a plasma of fixed temperature and density. Figure 9.3 shows the relaxation time for a number of temperatures for neon. Faster times are seen for the heavier gases. These curves are integrated for 1sec, the specified FPSS response time, to give the quantity of gas required. Quantities of a few 10's of Pa m^3 of neon and argon are sufficient and so define the size of reservoir required.

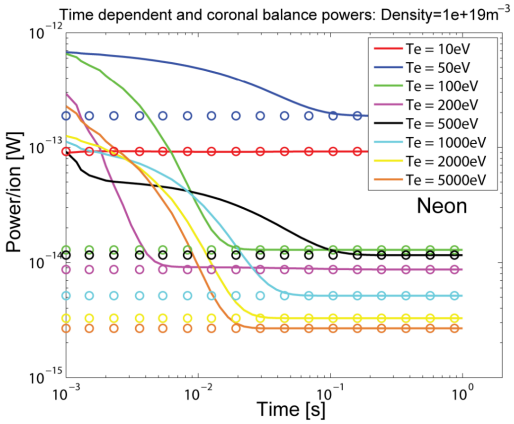

Figure 9.3: Relaxation time of neon to its coronal radiated power value for a set of target plasma temperatures.

Appendix A

ADAS-EU working visits to ITER

Date			Purpose
25-07-2010	–	30-07-2010	Upper port VUV CDR
15-11-2010	–	19-07-2010	Upper port X-ray CDR
29-11-2010	–	03-12-2010	ADAS course
13-02-2011	–	28-02-2011	
20-03-2011	–	25-03-2011	
13-04-2011	–	22-04-2011	Core and Divertor survey VUV CDR
18-07-2011	–	22-07-2011	
19-09-2011	–	23-09-2011	H-α CDR
04-12-2011	–	09-12-2011	

Table A.1: Summary of dates visits to ITER and participation in conceptual design reviews.

Bibliography

[1] EQDSK file format. Available from: https://fusion.gat.com/THEORY/efit/a_eqdsk.html

[2] G. V. Pereverzev and P. N. Yushmanov. 'ASTRA. Automated System for Transport Analysis in a Tokamak'. IPP-5/98, Max-Planck-Institut für Plasmaphysik (2002). Available from: http://edoc.mpg.de/display.epl?mode=doc&id=282186&col=33&grp=1311

[3] J. A. Crotinger, L. L. LoDestro, L. D. Pearlstein, A. Tarditi, T. A. Casper and E. B. Hooper. 'Corsica: A Comprehensive Simulation of Toroidal Magnetic-Fusion Devices'. Technical report (1997). LLNL Report UCRL-ID-126284. Available from: http://www.ntis.gov/search/product.aspx?ABBR=PB2005102154

[4] T. Cho, J. Kohagura, M. Hirata, Y. Sakamoto, T. Numakura, R. Minami, T. Sasuga, Y. Nishizawa, T. Okamura, T. Tamano, K. Yatsu, S. Miyoshi, K. Hirano and H. Maezawa. 'Effects of neutrons on semiconductor x-ray detectors including n-type Joint European Torus and p-type GAMMA 10 tomography detectors'. Rev. Sci. Instrum., **70**(1) (1999) 577–580. doi:10.1063/1.1149356

[5] J. Kohagura, T. Cho, M. Hirata, T. Numakura, R. Minami, H. Watanabe, T. Sasuga, Y. Nishizawa, M. Yoshida, S. Nagashima, T. Tamano, K. Yatsu, S. Miyoshi, K. Hirano and H. Maezawa. 'Effects of nuclear fusion produced neutrons on silicon semiconductor plasma X-ray detectors'. Nucl. Instrum. Methods Phys. Res., Sect. A, **477**(1–3) (2002) 215–219. doi:10.1016/S0168-9002(01)02020-4